

AB INITIO CALCULATIONS OF INTRAMOLECULAR EXCITON TRANSFER WITH
REDUCED MODES IN DONOR-BRIDGE-ACCEPTOR SPECIES

A Dissertation Presented to
the Faculty of the Department of Chemistry
University of Houston

In Partial Fulfillment
of the Requirements for the Degree
Doctor of Philosophy

By
Xunmo Yang
May 2016

*AB INITIO CALCULATIONS OF INTRAMOLECULAR EXCITON TRANSFER WITH
REDUCED MODES IN DONOR-BRIDGE-ACCEPTOR SPECIES*

Xunmo Yang

APPROVED:

Dr. Eric R. Bittner, Chairman

Dr. Vassiliy Lubchenko

Dr. Shoujun Xu

Dr. Don Coltart

Dr. Gila Stein
Department of Chemical and Biomolecular Engineering

Dean, College of Natural Sciences and Mathematics

Out yonder there was this huge world, which exists independently of us human beings and which stands before us like a great, eternal riddle, at least partially accessible to our inspection and thinking. The contemplation of this world beckoned as a liberation, and I soon noticed that many a man whom I had learned to esteem and to admire had found inner freedom and security in its pursuit. The mental grasp of this extra-personal world within the frame of our capabilities presented itself to my mind, half consciously, half unconsciously, as a supreme goal. Similarly motivated men of the present and of the past, as well as the insights they had achieved, were the friends who could not be lost.

- Albert Einstein

ACKNOWLEDGMENTS

I would like to offer my sincere gratitude to my thesis committee, Prof. Eric R. Bittner, Prof. Vassiliy Lubchenko, Prof. Shoujun Xu, Prof. Don Coltart, and Prof. Gila Stein for serving my committee and their help.

I would like to express my deepest gratitude to my advisor Prof. Eric Bittner for the continuous guidance and support of my Ph.D study and related research, especially for his patience and tolerance. I learn and do research in a bit uncommon way. Without his tolerance, I could not have finished my Ph.D study.

I would like to thank my fellow labmates: Allen Kelly, Svitlana Zaster, Hao Li, Kush Patel, Vladimir Lankevich, and Robert Paradez. They, especially Allen, helped me a lot to adapt to the new life here. I would like to thank Dmytro Bavzenko for his pretty thesis template.

I would like to express my gratitude to many great men in human history: Einstein, Darwin, Turing, Feynman, Hayek... The list is long. They are heroes in my heart. Bearing their thoughts and stories in mind, I never feel alone.

Last but not least, I would like to thank my mother, for the nurture and support she give me in so many years. I am indebted to her. Although she cannot understand my research - even a little bit, this thesis is for her.

AB INITIO CALCULATIONS OF INTRAMOLECULAR EXCITON TRANSFER WITH
REDUCED MODES IN DONOR-BRIDGE-ACCEPTOR SPECIES

An Abstract of a Dissertation Presented to
the Faculty of the Department of Chemistry
University of Houston

In Partial Fulfillment
of the Requirements for the Degree
Doctor of Philosophy

By
Xunmo Yang
May 2016

ABSTRACT

We present a new, fully *ab initio* approach for computing intramolecular charge and energy transfer rates. Using a time-convolutionless master equation approach, parameterized with couplings obtained from an accurate quantum chemical approach, we benchmark the approach against experimental results and predictions from Marcus theory for triplet energy transfer for a series of donor-bridge-acceptor systems. An important component of our analysis is the use of a projection operator scheme that parses out specific internal nuclear motions that accompany the electronic transition. Using an iterative Lanczos method, we concentrate the coupling between the electronic and nuclear degrees of freedom into a small number of reduced harmonic modes. We find that using only a single reduced mode—termed the “primary mode” or “Lanczos modes”, one obtains an accurate evaluation of the golden-rule rate constant and insight into the nuclear motions responsible for coupling the initial and final electronic states.

In particular, the irreducible representation of the primary mode reveals hidden details of the dynamics. For the cases considered here, the primary modes belong to totally symmetric irreducible representations of the donor and acceptor moieties. Upon investigating the molecular geometry changes following the transition, we propose that the electronic transition process can be broken into two steps, in the agreement of Born-Oppenheimer approximation: a fast excitation transfer occurs, facilitated by the “primary Lanczos mode” (PLM), followed by slow nuclear relaxation on the final electronic diabatic surface.

We apply the method to a larger, “star” molecule, that has been experimentally shown that its exciton transfer pathway can be radically modified by mode-specific infrared excitation of its vibrational mode. The primary mode and rate constants we obtain generally agree with the experiments.

CONTENTS

Contents vii

List of Figures ix

1	INTRODUCTION	1
1.1	INTRODUCTION	1
1.2	THEORETICAL APPROACH	3
1.2.1	<i>Model Hamiltonian</i>	3
1.2.2	<i>Non-Markovian Master Equation and Golden-Rule Rates</i>	5
1.2.3	<i>Adiabatic and Diabatic Representations</i>	6
1.2.4	<i>Edmiston-Ruedenberg Diabatization</i>	8
1.2.5	<i>Parameterization From Quantum Chemistry</i>	8
1.3	DETERMINING THE OPTIMAL ELECTRON-PHONON COUPLING COMPONENTS	10
1.3.1	<i>Lanczos Method</i>	12
1.4	SUMMARY	14
2	BENCHMARK AND PRIMARY MODE	16
2.1	INTRODUCTION	16
2.2	ASSUMPTION VALIDITY	17
2.3	ENERGY TRANSFER RATES IN DONOR-BRIDGE-ACCEPTOR SYSTEMS	17
2.4	DISCUSSION	24
3	PRIMARY MODE AND ITS RELATION TO TRANSFER DYNAMICS	26
3.1	INTRODUCTION	26
3.2	SYMMETRY OF THE PRIMARY LANCZOS MODES	26
3.3	LOCALIZED PROPERTY OF THE PRIMARY LANCZOS MODE	30
3.4	GEOMETRY CHANGE AND RELAXATION MODE	36
3.5	DISCUSSION	39
4	APPLICATION ON MORE COMPLEX MOLECULES	42
4.1	INTRODUCTION	42
4.2	EXPERIMENT RESULTS	42
4.3	THEORETICAL MODEL	46
4.4	RESULTS AND DISCUSSION	47
4.4.1	<i>Rate Constant</i>	47
4.4.2	<i>Primary Mode</i>	49
4.4.3	<i>Condon Approximation</i>	56

4.5 CONCLUSION	57
Appendices	59
A SAMPLE CODES	60
B SAMPLE Q-CHEM INPUT FOR OPTIMIZATION	68
C SAMPLE Q-CHEM INPUT FOR EDMISTON-RUEDENBERG DIABATIZATION AND FORCE CALCULATIONS	71
D GAUSSIAN INPUT FOR THE CSS STATE OF PTZ-PT-NAP	75
Bibliography	79

LIST OF FIGURES

- Figure 1 Sketch of Marcus parabolas for a model energy or charge transfer system. Labeled are the key parameters used to compute the Marcus rate constant (Eq. 1.1). Energies are given in eV and the collective nuclear displacement is dimensionless. 2
- Figure 2 Sketch of adiabatic and diabatic representations for two-state system. Compared to adiabatic representation, diabatic representation has smoother energy surfaces and couplings. 7
- Figure 3 Adiabatic energy curves and off-diagonal couplings computed along an interpolation coordinate between the $D^* - B - A$ and $D - B - A^*$ equilibrium geometries. V_{ab} is the off-diagonal coupling at each point along this coordinate. 18
- Figure 4 Comparison between predicted (TCLME) rate constants and the experimental rates from Ref. [18]. With exception of the methyl and D-2,6-ea bridged cases, the TCLME results are in good agreement with the experimental results. 20
- Figure 5 Primary coupling modes for (a) c-1,4ee and (b) d-2,6ae projected onto the atomic displacement coordinates. 21
- Figure 6 Convergence of the electronic coupling autocorrelation function (Eq. 2.1) with respect to number of reduced modes. 23
- Figure 7 Comparison between exact rate constant and its primary mode approximation. The blue points correspond to rates computed using only the primary mode and the renormalized energy for only that mode. The red points use the primary mode and the exact renormalized energies. 24
- Figure 8 Projection of PLMs onto (a) benzaldehyde in c-1,4ee (b) symmetrized naphthalene in c-1,4ee, (c) benzaldehyde in d-2,6ae and (d) symmetrized naphthalene in d-2,6ae. The normal modes are listed from low to high frequency and the irreducible representations of the dominant modes are color-coded. The assigned IRs for naphthalene are exact whereas the IRs are only approximate for benzaldehyde. 28
- Figure 9 The correlation functions of projected modes for c-1,4ee with the naphthalene moiety replaced by (a) phenyl ring and (b) anthracene, with their PLMs shown in (c) and (d). 30
- Figure 10 The (a) (A_u) HOMO and (b) (B_{2g})LUMO of naphthalene. 31
- Figure 11 Projections of the PLM onto the normal modes of (a) c-1,4ee and (b) d-2,6ae. 32

- Figure 12 Projection of PLMs onto unsymmetrized naphthalene for (a) c-1,4ee and (b) d-2,6ae. They are almost same to Fig. 8(b) and (d) except for a mode with B_{2u} symmetry in c-1,4ee. Embedded are the most significant modes, namely, the 33rd modes 33
- Figure 13 Correlation functions for different combinations of normal modes are shown for (a) c-1,4ee and (b) d-2,6ae. The “exact” ones refer are for the PLMs. “NfBf” is the mode made up from all normal modes of both the donor and acceptor sites. The designation “NxBy” indicates that the correlation function was constructed using x most significant normal modes on naphthalene and y most significant ones on benzaldehyde. Plots (c) and (d) show the relative error in rate constants calculated for various combinations of normal modes compared to the exact result of c-1,4ee (c) and d-2,6ae (d), respectively. 35
- Figure 14 Projections of the geometry change between initial and final states onto the normal modes of (a) benzaldehyde and (b) naphthalene sites in c-1,4ee, and d-2,6ae in (c) and (d). Except for some low frequency modes, they are similar to the projections of PLM. 37
- Figure 15 Projections of the geometry change between initial and final states onto the normal modes of (a) c-1,4ee and (b) d-2,6ae. They are both dominated by single mode, the relaxation mode (RM), which is embedded. 38
- Figure 16 Correlation functions of relaxation mode (RM), PLM, geometry change (GC), and geometry change with the RM component eliminated for (a) c-1,4ee and (b) d-2,6ae. The exact rate is computed using the full set of normal modes. 40
- Figure 17 Relative comparison of the rate constants computed using different sets of reduced modes. blue = c-1,4ee, gold =d-2,6ae. 41
- Figure 18 a. Molecular structure of PTZ-CH₂-Pt-NAP, PTZ-Pt-NAP and OMe-PTZ-Pt-NAP, from left to right. b. Energy level diagrams for the ET process, with the lifetimes and the driving force (ΔG) of CT → CSS transfer indicated. Adapted with permission from Ref. [44]. 43
- Figure 19 The sketch of ET pathways. For PTZ-CH₂-Pt-NAP, the CT → CSS step can be fully suppressed by intermediate infrared excitation. Reprinted with permission from Ref. [44]. 44

- Figure 20 Calculated energies of the CT (black), CSS (blue) and ^3NAP (red) states along the NAP side $\text{C}\equiv\text{C}$ coordinate in the ground state geometries of the molecules studied, in CH_2Cl_2 . a, PTZ- CH_2 -Pt-NAP. b, PTZ-Pt-NAP. c, OMe-PTZ-Pt-NAP. The first and second vibrational energy levels for the asymmetric $\text{C}\equiv\text{C}$ stretch are shown for the CT state. The energy gaps from ν_0 to the intersection between CT and CSS are shown in the insets. There is a clear trend concerning the energy gap: PTZ- CH_2 -Pt-NAP < PTZ-Pt-NAP < OMe-PTZ-Pt-NAP, reflecting the trend experimentally observed in the efficiency of the infrared control effect. Reprinted with permission from Ref. [44]. 45
- Figure 21 The energy diagram of triplet states at ^3NAP and CT state geometries. The electron/hole distribution are shown as well (green for electron, blue for hole). The arrows indicate the transitions we calculate. 48
- Figure 22 Comparisons between theoretical rate constants and the experimental rates. Experimental rates are calculated as yield of product/lifetime of reactant, using values from Ref. [44]. The “Marcus” rates are calculated using Marcus theory with the diabatic couplings at according geometries. The “Marcus (mean V)” rates are calculated using mean diabatic couplings along the interpolated coordinate in Fig. 27. Similarly, the “TCLME” and “TCLME (mean V)” rates are calculated using the TCLME approach, with all normal modes used. The “PLM” rates are calculated using only the primary mode. Our approach performs better than Marcus theory. The CT geometry gives good “exact” results, its primary mode rates also agree well. While for the ^3NAP geometry, using mean value of diabatic couplings along the reaction coordinate significantly improves the performance. 50
- Figure 23 Correlation functions of various numbers of projected modes, compared to exact correlation, for (a) CSS \rightarrow ^3NAP at ^3NAP geometry, (b) CT \rightarrow ^3NAP at ^3NAP geometry, (c) CT \rightarrow ^3NAP at CT geometry, and (d) CT \rightarrow CSS at CT geometry. 51
- Figure 24 Projection of primary mode of (a) CSS \rightarrow ^3NAP , (b) CT \rightarrow ^3NAP calculated at ^3NAP geometry onto the normal modes of ^3NAP . Embedded molecule shows the atomic displacement vectors of primary mode. If we focus on the $\text{C}\equiv\text{C}$ bonds, PLMs are like PTZ-Ph- $\text{C}\equiv\text{C}$ -Pt- $\overset{\leftarrow}{\text{C}}\equiv\overset{\rightarrow}{\text{C}}$ -NAP in (a) and PTZ-Ph- $\overset{\leftarrow}{\text{C}}\equiv\overset{\rightarrow}{\text{C}}$ -Pt- $\overset{\leftarrow}{\text{C}}\equiv\overset{\rightarrow}{\text{C}}$ -NAP in (b). 53
- Figure 25 Projection of primary mode of (a) CT \rightarrow ^3NAP , and (b) CT \rightarrow CSS calculated at CT geometry onto the normal modes of CT. Embedded molecule shows the atomic displacement vectors of primary mode. If we focus on the $\text{C}\equiv\text{C}$ bonds, PLMs are like PTZ-Ph- $\overset{\leftarrow}{\text{C}}\equiv\overset{\rightarrow}{\text{C}}$ -Pt- $\overset{\leftarrow}{\text{C}}\equiv\overset{\rightarrow}{\text{C}}$ -NAP in (a) and PTZ-Ph- $\overset{\leftarrow}{\text{C}}\equiv\overset{\rightarrow}{\text{C}}$ -Pt- $\overset{\leftarrow}{\text{C}}\equiv\overset{\rightarrow}{\text{C}}$ -NAP in (b). 54

- Figure 26 From top to bottom: the displacement vectors of the 174th, 175th mode of ${}^3\text{NAP}$ state, the 174th, 175th mode of CT state. For clarity, bonds are not shown. They are all the stretching modes of single $\text{C}\equiv\text{C}$ bond, look like PTZ-Ph-C \equiv C-Pt-C $\overset{\leftrightarrow}{\equiv}$ C-NAP in (a), PTZ-Ph-C \equiv C-Pt-C $\overset{\leftrightarrow}{\equiv}$ C-NAP in (b), PTZ-Ph- $\overset{\leftarrow}{\text{C}}$ \equiv $\overset{\rightarrow}{\text{C}}$ -Pt- $\overset{\rightarrow}{\text{C}}$ \equiv $\overset{\leftarrow}{\text{C}}$ -NAP in (c), and PTZ-Ph- $\overset{\leftarrow}{\text{C}}$ \equiv $\overset{\rightarrow}{\text{C}}$ -Pt- $\overset{\leftarrow}{\text{C}}$ \equiv $\overset{\rightarrow}{\text{C}}$ -NAP in (d). 55
- Figure 27 Diabatic coupling values along the interpolation from the ${}^3\text{NAP} \rightarrow \text{CT}$ geometries. State o and 1o stand for the ${}^3\text{NAP}$ and the CT state, respectively. 57

1

INTRODUCTION

1.1 INTRODUCTION

Energy and electronic transport plays a central role in a wide range of chemical and biological systems. It is the fundamental mechanism for transporting the energy of an absorbed photon to a reaction center in light harvesting systems and for initiating a wide range of photo-induced chemical processes, including vision, DNA mutation, and pigmentation. The seminal model for calculating electron transfer rates was developed by Marcus in the 1950's[1–3].

$$k_{Marcus} = \frac{2\pi}{\hbar} |V_{ab}|^2 \frac{1}{\sqrt{4\pi k_B T \lambda}} e^{-(\lambda + \Delta\epsilon)^2 / 4\lambda k_B T}. \quad (1.1)$$

where λ is energy required to reorganize the environment following the transfer of an electron from donor to acceptor. and $\Delta\epsilon$ is the driving force for the reaction, as illustrated in Fig. 1. If we assume that the nuclear motions about the equilibrium configurations of the donor and acceptor species is harmonic, the chemical reactions resulting from energy or charge transfer events can be understood in terms of intersecting diabatic potentials as sketched. The upper and lower curves are the adiabatic potential energy surfaces describing the nuclear dynamics resulting from an energy or charge transfer event, taking the geometry of the donor state as the origin.

o Part of this chapter has been published in Xunmo Yang and E. R. Bittner, The Journal of Physical Chemistry A **118**, 5196 (2014)

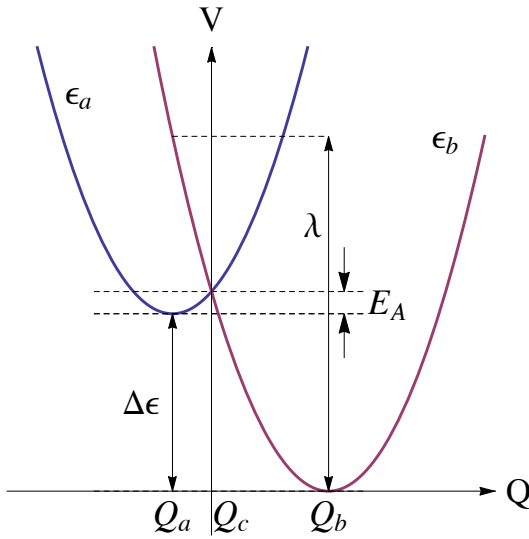


Figure 1.: Sketch of Marcus parabolas for a model energy or charge transfer system. Labeled are the key parameters used to compute the Marcus rate constant (Eq. 1.1). Energies are given in eV and the collective nuclear displacement is dimensionless.

As the transfer occurs by crossing an energy barrier, the transfer rate can be expected to be in the Arrhenius form

$$k \propto e^{-E_A/k_B T}, \quad (1.2)$$

with E_A as the activation energy. Using $E_A = (\lambda + \Delta\epsilon)^2/4\lambda$ we can relate the activation energy to both the reorganization energy and driving force, $-\Delta\epsilon$. One of the most profound predictions of the theory is that as the driving force increases, the transfer rate reaches a maximum and further increases in the driving force lead to lower reaction rates, termed the inverted regime. The inverted region is unequivocally substantiated by Miller *et al.* [18] in a series experiments of intramolecular transfer. Part of their work is used as the experimental benchmark of our model in Chapter 2 and 3.

A number of years ago, our group developed a time-convolutionless master equation approach for computing state-to-state rates in which the coupling between states depends upon the nuclear

1.2 THEORETICAL APPROACH

coordinates[4]. This approach incorporates a fully quantum mechanical treatment of both the nuclear and electronic degrees of freedom and recovers the well-known Marcus expression in the semiclassical limit. The model is parameterized by the vibrational normal mode frequencies, and the electronic energies and energy derivatives at a reference configuration. The approach has been used by our group to compute state-to-state transition rates in semi-empirical models for organic semiconducting light-emitting diode and photovoltaics [5–8]. Our work here represents the first time this approach has been used within the context of a fully *ab initio* quantum chemical model. As such, this present work provides an important benchmark of the approach since all parameters will be determined using state-of-the-art quantum chemical methods and results compared to both theoretical and experimental rates.

1.2 THEORETICAL APPROACH

Below we give a detailed description of our methods.

1.2.1 *Model Hamiltonian*

We consider a generic model for n electronic states coupled linearly to a phonon bath. Taking the electronic ground state of the system as a reference and assuming that the electronic states are coupled linearly to a common set of modes, we arrive at a generic form for the Hamiltonian, here written for two coupled electronic states:

$$H = \begin{pmatrix} \epsilon_1 & 0 \\ 0 & \epsilon_2 \end{pmatrix} + \begin{pmatrix} g_{11} & g_{12} \\ g_{21} & g_{22} \end{pmatrix} \cdot \mathbf{q} + \frac{\mathbf{p}^2}{2} + \frac{1}{2} \mathbf{q}^T \cdot \Omega \cdot \mathbf{q}. \quad (1.3)$$

1.2 THEORETICAL APPROACH

Here, the first term contains the electronic energies, ϵ_1 and ϵ_2 computed at a reference geometry—typically that of the donor or acceptor state. The second term represents the linearized coupling between the electronic and nuclear degrees of freedom given in terms of the mass-weighted normal coordinates \mathbf{q} . The equation assumes the potentials for the excited states are parabolic. This is usually valid in the reaction region, as we will show in next several chapters. The diagonal terms give the adiabatic displacement forces between the reference geometry and the two states. If we choose one of the states as the reference state, then either \mathbf{g}_{11} or \mathbf{g}_{22} will vanish. The remaining two terms correspond to the harmonic motions of the nuclear normal modes, given here in mass-weighted normal coordinates. In the normal mode basis, the Hessian matrix, Ω , is diagonal with elements corresponding to the normal mode frequencies, ω_j^2 .

We now separate Eq. 1.3 into diagonal and off-diagonal terms

$$\hat{H} = \hat{H}_o + \hat{V} \quad (1.4)$$

and perform a polaron transform using the unitary transformation [4, 9, 10].

$$\begin{aligned} U &= e^{-\sum_{ni} \frac{g_{nni}}{\hbar\omega_i} |n\rangle\langle n| (a_i^\dagger - a_i)} \\ &= \sum_n |n\rangle\langle n| e^{-\sum_i \frac{g_{nni}}{\hbar\omega_i} (a_i^\dagger - a_i)} \end{aligned} \quad (1.5)$$

under which the transformed Hamiltonian is written in terms of the diagonal elements

$$\tilde{H}_0 = U^{-1} H_0 U = \sum_n \tilde{\epsilon}_n |n\rangle\langle n| + \sum_i \hbar\omega_i a_i^\dagger a_i, \quad (1.6)$$

with the renormalized electronic energies,

$$\tilde{\epsilon}_n = \epsilon_n - \sum_i \frac{g_{nni}^2}{\hbar\omega_i}, \quad (1.7)$$

1.2 THEORETICAL APPROACH

and off-diagonal terms,

$$\hat{V}_{nm} = \sum_i g_{nni} \left(a_i^\dagger + a_i - \frac{2g_{nni}}{\hbar\omega_i} \right) e^{\sum_j \frac{(g_{nnj}-g_{mmj})}{\hbar\omega_j} (a_j^\dagger - a_j)}. \quad (1.8)$$

In the transformed (or dressed) picture the electronic transition from state $|n\rangle$ to $|m\rangle$ is accompanied by the excitations of all the normal modes. Following the conventional notations in this field, we refer to all harmonic nuclear motions as phonons. Transforming to the interaction representation and performing a trace over the phonons gives the spectral density in terms of the autocorrelation of the electron-phonon coupling operators.

$$S_{nm}(\tilde{\omega}) = \int_{-\infty}^{\infty} dt e^{-i\tilde{\omega}t} \langle \hat{V}_{nm}(t) \hat{V}_{mn}(0) \rangle. \quad (1.9)$$

Here, $\hat{V}_{nm}(t)$ is the electron-phonon coupling term in the Heisenberg representation and $\langle \dots \rangle$ denotes a thermal average over the vibrational degrees of freedom. The derivation and explicit form for the kernel in Eq. 1.9 is quite lengthy and is given in Ref. [4].

1.2.2 Non-Markovian Master Equation and Golden-Rule Rates

In Ref. [4], Pereverzev and Bittner derived a non-Markovian, time-convolutionless form of the Pauli master equation (TCLME) for general system described by Eq. 1.3.

$$\frac{dP_n}{dt} = \sum_{m \neq n} W_{nm}(t) P_m(t) - \sum_{m \neq n} W_{mn}(t) P_n(t) \quad (1.10)$$

where the time-dependent rates are given by

$$W_{nm}(\tau) = 2\text{Re} \int_0^\tau dt \langle \hat{V}_{nm}(0) \hat{V}_{mn}(t) \rangle e^{-i\tilde{\omega}_{nm}t}. \quad (1.11)$$

1.2 THEORETICAL APPROACH

In the limit that $\tau \rightarrow \infty$, Eq. 1.11 gives the Fermi's Golden Rule expression for the transition rate,

$$k_{nm} = 2\text{Re} \int_0^\infty dt \langle \hat{V}_{nm}(0) \hat{V}_{mn}(t) \rangle e^{-i\tilde{\omega}_{nm} t}. \quad (1.12)$$

At this point it is useful to connect the various terms in the phonon-dressed Hamiltonian with specific physical parameters. First, the reorganization energy is given by

$$\lambda_{nm} = \sum_j \frac{(g_{nnj} - g_{mmj})^2}{\omega_j} = \sum_j \hbar\omega_j S_j \quad (1.13)$$

where the $\{S_j\}$ are the Huang-Rhys factors for each phonon mode. These are related to the Franck-Condon factor describing the overlap between the $v_j = 1$ vibronic state in one electronic state with the $v_j = 0$ vibronic state in the other. Likewise, the energy difference between the renormalized energy gaps is related to the driving force of the state-to-state transition,

$$\Delta E_{nm} = \tilde{\epsilon}_n - \tilde{\epsilon}_m. \quad (1.14)$$

We first developed the approach about 10 years ago. However, the difficulty in using this approach is that it requires both diagonal (g_{nn}) and off-diagonal (g_{nm}) derivative couplings between adiabatic states. In the following section, we discuss how we have used the Edmiston-Ruedenberg (ER) localization scheme [11] to estimate the couplings. We also present how one can construct a reduced set of harmonic modes that fully capture the electron/nuclear coupling.

1.2.3 Adiabatic and Diabatic Representations

There are two common ways to represent the Hamiltonian, adiabatic and diabatic representations, as sketched in Fig. 2. The way we represent the Hamiltonian in Eq. 1.3 is adiabatic representation,

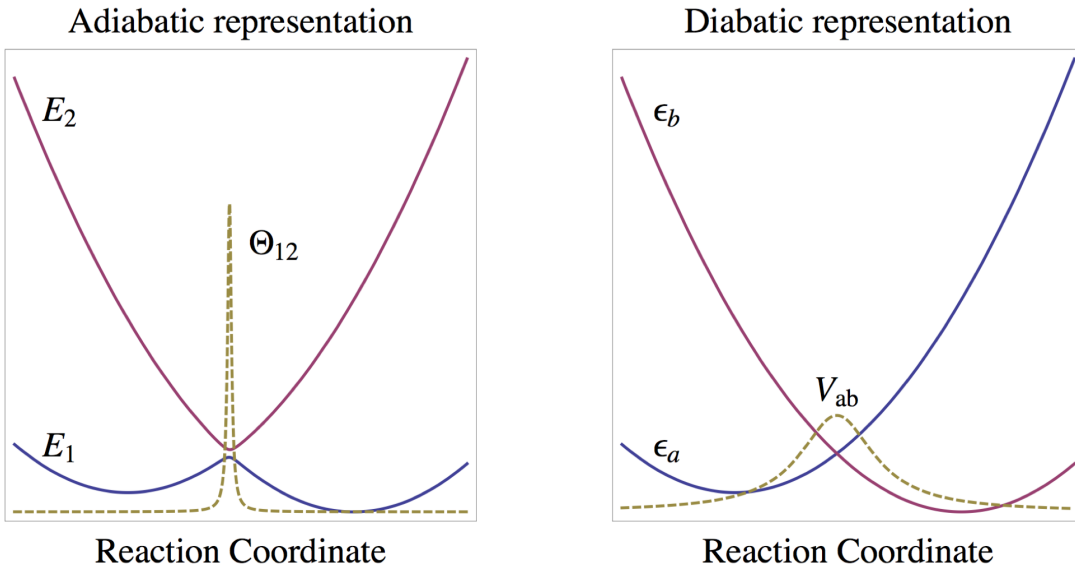


Figure 2.: Sketch of adiabatic and diabatic representations for two-state system. Compared to adiabatic representation, diabatic representation has smoother energy surfaces and couplings.

where states are the eigenstates of molecule, and hence can be directly calculated in *ab initio* quantum chemistry software. However, the off-diagonal couplings in adiabatic representations (g_{ij} in Eq. 1.3) are derivative couplings, which are difficult to compute. Even worse, the couplings change radically near avoided crossing. A workaround is switching to diabatic representation, where the Hamiltonian is written as

$$H_{dia} = U^T H_{adia} U = \begin{pmatrix} \epsilon_a(\mathbf{R}) + T'_n(\mathbf{R})_{11} & V_{ab} \\ V_{ab} & \epsilon_b(\mathbf{R}) + T'_n(\mathbf{R})_{22} \end{pmatrix}. \quad (1.15)$$

The diabatic representation has several advantages. First, sharp derivative couplings in adiabatic representations are transformed to smoother static diabatic couplings, V_{ab} . Second, potential energy surfaces are smoothed and avoided crossing is eliminated.

1.2 THEORETICAL APPROACH

The problem now is how to obtain the transformation matrix

$$U = \begin{pmatrix} \cos \theta & \sin \theta \\ -\sin \theta & \cos \theta \end{pmatrix}. \quad (1.16)$$

There are many methods available [12]. Here we introduce the Edmiston-Ruedenberg diabatization approach.

1.2.4 *Edmiston-Ruedenberg Diabatization*

A straightforward way to construct diabatic states is to eliminate derivative coupling mathematically, namely, to solve

$$\langle \phi_i(\mathbf{r}; \mathbf{R}) | \nabla_{\mathbf{R}} | \phi_j(\mathbf{r}; \mathbf{R}) \rangle = 0. \quad (1.17)$$

However, it is computationally very expensive, and exact solution do not usually exist [13].

Another category of diabatization methods is based on physical intuition, with ER diabatization being one of them. The ER diabatization is based on the idea that good diabatic states are supposed to be localized, so the approach defines the diabatic states by maximizing the total electron repulsion

$$f_{ER} = \sum_k^{N_{states}} \iint d\mathbf{r}_1 d\mathbf{r}_2 \frac{\langle \phi_k | \hat{\rho}(r_1) | \phi_k \rangle \langle \phi_k | \hat{\rho}(r_2) | \phi_k \rangle}{\| \mathbf{r}_1 - \mathbf{r}_2 \|}. \quad (1.18)$$

1.2.5 *Parameterization From Quantum Chemistry*

In order to obtain the final form of our target Hamiltonian, we assume the diabatic potentials are a good approximation to the actual adiabatic potentials.

1.2 THEORETICAL APPROACH

When the adiabatic (and diabatic) energy minima are far enough away from the crossing points and the mixing angles between the diabatic and adiabatic states is small, we can use the gradients of the adiabatic potentials to approximate the diabatic potentials. Thus, if we perform calculations at the optimized geometry of the final acceptor state (*i. e.* about Q_2 in Fig. 1), we can write the Hamiltonian as

$$H_{dia,e} = \begin{pmatrix} \epsilon_1 & V_{12} \\ V_{21} & \epsilon_2 \end{pmatrix} + \begin{pmatrix} 0 & 0 \\ 0 & 1 \end{pmatrix} \mathbf{g}_{22} \cdot \mathbf{q} + H_{osc}, \quad (1.19)$$

where H_{osc} is the harmonic oscillator Hamiltonian for the vibrational normal modes. The linear assumption amounts to performing a series expansion of the full, multi-dimensional coupling term and keeping only the lowest order terms. Systematic improvement can be made by including higher-order (e.g. quadratic) off-diagonal couplings. However, this would involve a substantial increase in the complexity of the theory. The linear assumption is reasonable so long as the mixing angle is small, as verified by the benchmark calculations presented below.

We obtain the diabatic couplings V_{12} and the mixing angle θ via ER localization and transform the electronic Hamiltonian from the adiabatic basis to the diabatic basis *viz.*

$$H_{dia} = \begin{pmatrix} \cos \theta & -\sin \theta \\ \sin \theta & \cos \theta \end{pmatrix} \begin{pmatrix} \epsilon_1 & 0 \\ 0 & \epsilon_2 \end{pmatrix} \begin{pmatrix} \cos \theta & \sin \theta \\ -\sin \theta & \cos \theta \end{pmatrix}. \quad (1.20)$$

The diabatic coupling is then given by

$$V_{ab} = \frac{1}{2} \sin 2\theta (\epsilon_2 - \epsilon_1). \quad (1.21)$$

1.3 DETERMINING THE OPTIMAL ELECTRON-PHONON COUPLING COMPONENTS

We then diagonalize the electronic part and transform the electron/nuclear coupling back into the adiabatic basis. In doing so, we obtain the Hamiltonian in the form given in Eq. 1.3

$$\begin{aligned} H &= U^T H_{dia} U \\ &= \begin{pmatrix} E_1 & 0 \\ 0 & E_2 \end{pmatrix} + \begin{pmatrix} \sin^2 \theta & \frac{1}{2} \sin 2\theta \\ \frac{1}{2} \sin 2\theta & \cos^2 \theta \end{pmatrix} \mathbf{g}_{22} \cdot \mathbf{q} \\ &+ H_{osc}. \end{aligned} \quad (1.22)$$

1.3 DETERMINING THE OPTIMAL ELECTRON-PHONON COUPLING COMPONENTS

While the Marcus expression is elegant in its simplicity in requiring three parameters that can be obtained experimentally, it masks a wealth of detail that underlie the quantum transition. Considerable insight into the state-to-state dynamics can be revealed by examining such motions. However, until this work a general systematic approach for determining such motions did not exist. Our approach is based on earlier work by our group [14] and Burghardt *et al.* [15–17]. Central to the theory is that there exists a collective nuclear displacement coordinate that connects the initial geometry of the donor to the final geometry of the acceptor.

Generally speaking, this collective coordinate involves all nuclear degrees of freedom. However, the form of the electronic Hamiltonian in Eq. 1.3 suggests that there exists a subset of motions that are specific modes that capture the majority of the electronic/nuclear coupling and give the dominant contribution to the collective reaction coordinate. Within the linearized approximation for the electronic/nuclear coupling, we can write a force tensor

$$\mathbf{F} = \begin{pmatrix} \mathbf{g}_{11} & \mathbf{g}_{12} \\ \mathbf{g}_{21} & \mathbf{g}_{22} \end{pmatrix} \quad (1.23)$$

where $\mathbf{F} \cdot \mathbf{q}$ is the electronic/nuclear coupling term in Eq. 1.3. If we consider each unique element $\{\mathbf{g}_{11}, \mathbf{g}_{12}, \mathbf{g}_{22}\}$ to be linearly independent, but non-orthogonal force vectors, one can develop a projection operator scheme to parse the N -dimensional linear vector space spanned by the mass-weighted normal mode vectors into two subspaces: one spanned by three vectors describing the coupling between the electronic states and the other spanned by the remaining $N - 3$ dimensional space spanned by motions that do not couple the electronic states. This subspace can be generated by defining a projection operator

$$\mathbf{P} = \sum'_{\alpha\beta} (\mathbf{S}^{-1})_{\alpha\beta} \mathbf{g}_\alpha \otimes \mathbf{g}_\beta \quad (1.24)$$

in which the summation is limited to linearly independent vectors. Here $\mathbf{S}_{\alpha\beta} = \mathbf{g}_\alpha \cdot \mathbf{g}_\beta$, \otimes is outer product, and \mathbf{I} is unitary operator. This $N \times N$ matrix projects out all normal modes that are directly coupled to the electronic degrees of freedom and its complement $\mathbf{Q} = \mathbf{I} - \mathbf{P}$ projects out all modes not directly coupled. By diagonalizing the matrix

$$\mathbf{K} = \mathbf{P} \cdot \Omega \cdot \mathbf{P} + \mathbf{Q} \cdot \Omega \cdot \mathbf{Q} \quad (1.25)$$

we obtain a transformation, \mathbf{M} , between the normal coordinates and a new set of orthogonal coordinates. Both $\mathbf{P} \cdot \Omega \cdot \mathbf{P}$ and $\mathbf{Q} \cdot \Omega \cdot \mathbf{Q}$ are $N \times N$ matrices. However, for a two-state system, the former will have exactly 3 non-trivial eigenvalues, $\{\alpha_p\}$, with corresponding eigenvectors, $\{M_p\}$, whereas the latter will have exactly $N_r = N - 3$ non-trivial eigenvalues, $\{\alpha_q\}$, and corresponding eigenvectors, $\{M_q\}$. This the full $N \times N$ transformation is formed by joining the non-trivial vectors from the two respective subspaces $\mathbf{M} = \{M_p, M_q\}$. The transformed electron-phonon coupling constants are given by projecting the couplings in the normal mode basis on to the new basis.

$$\mathbf{g}'_{ab} = \mathbf{M}_p \cdot \mathbf{g}_{ab} \cdot \mathbf{M}_q \quad (1.26)$$

By examining the types of molecular motions that compose the \mathbf{M}_p subspace, we can gain a deeper understanding of the specific classes of internal motion that are directly involved with the electron transfer process. In addition, we can gain a computational advantage since presumably this reduced set of modes give the dominant contribution to the electron-phonon coupling and autocorrelation function given as the kernel in Eq. 1.12.

1.3.1 Lanczos Method

It is crucial to notice that the vectors given in Eq. 1.22 are *not linearly independent*. Consequently, special care must be taken to generate the reduced sub-space. To facilitate this, we develop an iterative Lanczos approach, taking the normalized vector $\mathbf{v}_1 = \mathbf{g}_{22}$ as a starting point.

As above, we initialize each step indexed by k , by defining a projection operator

$$\mathbf{P}_k = \mathbf{v}_k \otimes \mathbf{v}_k \quad (1.27)$$

and its complement $\mathbf{Q}_k = \mathbf{I} - \mathbf{P}_k$. k -th mode. We then project the Hessian matrix Ω into each subspace *viz.*

$$\Omega_p = \mathbf{P}_k \cdot \Omega \cdot \mathbf{P}_k \quad \& \quad \Omega_q = \mathbf{Q}_k \cdot \Omega \cdot \mathbf{Q}_k \quad (1.28)$$

and diagonalize each to obtain eigenvalues and eigenvectors $\{\alpha_p, \mathbf{M}_p\}$ and $\{\alpha_q, \mathbf{M}_q\}$ respectively. As above, Ω_p and Ω_q are $N \times N$ matrices. The first set will have a single non-trivial eigenvalue and the second set will have $N - k$ non-trivial eigenvalues. As above we collect the non-trivial eigenvectors associated with each to form the orthogonal transformation matrix

$$\mathbf{M}_k = \{\mathbf{M}_p, \mathbf{M}_q\}, \quad (1.29)$$

and again transform the full Hessian Ω into this new vector space to form the $N \times N$ matrix Ω' .

At each step in the iteration, the transformed Hessian, Ω' is in the form of a $k \times k$ tri-diagonal submatrix in the upper-left part of the matrix and a diagonal submatrix in the lower-right. For example, after $k = 3$ iterations, the Hessian matrix takes the form:

$$\Omega' = \begin{pmatrix} \alpha_1 & b_1 & 0 & & & & 0 \\ b_1 & \alpha_2 & b_2 & & & & \\ 0 & b_2 & \alpha_3 & c_{k+1} & c_{k+2} & \cdots & c_N \\ & & c_{k+1} & \alpha_{k+1} & & & 0 \\ & & & c_{k+2} & & \alpha_{k+2} & \\ & & & \vdots & & \ddots & \\ 0 & c_N & 0 & & & & \alpha_N \end{pmatrix}. \quad (1.30)$$

We note that only the k -th mode is coupled the $N - k$ remaining modes. Since all of the transformations are orthogonal, diagonalizing Ω' at any point returns the original Hessian matrix.

To continue iterating, we take the k -th row of Ω' and zero the first k elements

$$\mathbf{e} = \{0, \dots, 0, c_{k+1}, c_{k+2}, \dots, c_N\}.$$

This is the coupling between the upper tridiagonal block and the lower diagonal block. We thus obtain a new vector

$$\mathbf{v}_{k+1} = \mathbf{e} \cdot \mathbf{M}$$

which is then reintroduced into the iteration scheme.

At any point along the way, we can terminate the iteration and obtain a reduced set of couplings. Since the Lanczos approach uses the power method for finding the largest eigenvector of a matrix, it converges first upon the vector with the largest electron/nuclear coupling—which we refer to

1.4 SUMMARY

as the “primary mode”. Subsequent iterations produce reduced modes with progressively weaker electron/nuclear couplings and the entire process can be terminated after a few iterations. After k -steps, the final electron-phonon couplings are then obtained by projecting the original set of couplings (in the normal mode basis) into the final vector space.

For the first iteration, \mathbf{v}_1 is parallel to the bare electron-phonon coupling vector \mathbf{g}_{22} and the associated frequency is $\mathbf{v}_1 \cdot \Omega \cdot \mathbf{v}_1$. The subsequent iterations introduce corrections to this via phonon-phonon coupling mediated via the electronic couplings. For example, for the $k = 3$ iteration, we would determine the active vector space in terms of the upper-left 3×3 block of the matrix in Eq. 1.30.

$$\Omega'_3 = \begin{pmatrix} \alpha_1 & b_1 & 0 \\ b_1 & \alpha_2 & b_2 \\ 0 & b_2 & \alpha_3 \end{pmatrix} \quad (1.31)$$

Diagonalizing Ω'_3 returns a set of frequencies and associated eigenvectors which are then used to compute the electron-phonon couplings in this reduced active space. After $N - 1$ iterations, Ω' is a fully tridiagonal matrix and diagonalizing this returns the original normal mode basis.

1.4 SUMMARY

The theory presented here consists of two parts. One is the use of a diabatization scheme for determining donor and acceptor states in a molecular unit. The other is a projection scheme enables us to analyze the contribution of vibrations in reactions. Similar decomposition schemes have been presented by Burghardt [15–17] and the approach used here builds upon the method given in Ref. [14], but they decomposed normal modes into a 3 by 3 hierarchy, while we are able to get projected modes 1 by 1. This facilitates the analysis of dominating nuclear motions in transfer.

1.4 SUMMARY

In Chapter 2 we benchmark the approach by computing the triplet energy transfer rates for a series of donor-bridge-acceptor molecules originally studied by Closs[18]. The triplet energy transfer rates computed using our approach compare well against both the experimental rates and with more recent theoretical rates presented by Subotnik *et al.* [19–21]. Then we use the projection operator scheme to parse out specific internal nuclear motions that accompany the electronic transition. By analyzing the electron-phonon couplings, we can discern a reduced set of motions that are responsible for coupling between the donor and acceptor states.

In Chapter 3 we analyze the irreducible representations of the dominant contributions of these reduced modes and find that for the cases considered here, they belong to totally symmetric irreducible representations of the donor and acceptor moieties. Upon investigating the molecular geometry changes following the transition, we propose that the electronic transition process can be broken into two steps, in the agreement of Born-Oppenheimer approximation: a fast excitation transfer occurs, facilitated by the “primary Lanczos mode” (PLM), followed by slow nuclear relaxation on the final electronic diabatic surface.

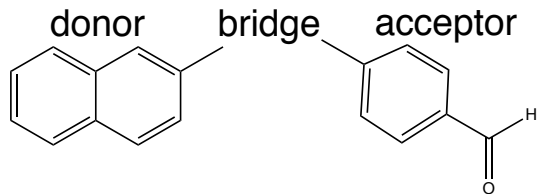
In Appendices we provide some sample codes and input files for analysis.

2

BENCHMARK AND PRIMARY MODE

2.1 INTRODUCTION

In this chapter we focus on the rates of triplet exchange between a naphthalene donor and a benzaldehyde acceptor linked by a variety of bridging units.



Triplet energy exchange in these systems occurs via the through-space Dexter mechanism [22]. This is a short-ranged interaction involving the simultaneous exchange of two electrons between the donor and acceptor moieties. Systems such as these formed the basis of a series of experiments by Closs and Miller [18] in which they verified the existence of the Marcus “inverted regime” - the very negative ΔG domain where transfer becomes slower - and serve as crucial benchmarks for testing new theoretical models for computing energy and charge transfer rates [19–21]. The molecules are sketched in Table. 1.

The chapter is arranged in this way. First we examine the validity of the assumptions in our method. Then we apply the method to obtain theoretical transfer rate constants, and compare these

o Part of this chapter has been published in Xunmo Yang and E. R. Bittner, Intramolecular Charge- and Energy-Transfer Rates with Reduced Modes: Comparison to Marcus Theory for Donor–Bridge–Acceptor Systems. *The Journal of Physical Chemistry A* **118**, 5196 (2014)

2.2 ASSUMPTION VALIDITY

to experimental results. Finally, we use the projection scheme to find the primary modes in the reactions.

2.2 ASSUMPTION VALIDITY

Our method employs two assumptions. First is that the diabatic surfaces are harmonic. Second, the Condon approximation is valid, namely, the diabatic couplings are independent of nuclear coordinates in the region where the reaction occurs. In Fig. 3 we show the computed adiabatic potential curves and off-diagonal couplings along an interpolation coordinate connecting the equilibrium geometries of the donor and acceptor states for the d-2,6ae molecule. The dashed curve gives the parabolic approximation to the lower potential curves. Along this coordinate, the off-diagonal coupling is small and essentially linear and the parabolic approximation provides a good approximation to the actual potential. This indicates that the assumptions in our model Hamiltonian are generally robust for the systems we consider herein.

2.3 ENERGY TRANSFER RATES IN DONOR-BRIDGE-ACCEPTOR SYSTEMS

Using the ER localization approach explained in Section 1.2.4, all parameters needed for our model can be obtained from standard quantum chemical packages. The vertical energies, ϵ_a and ϵ_b are obtained from single point CI(S) calculations at a given reference geometry. We then project the energy gradients onto the vibrational normal coordinates to obtain the electron-phonon coupling constants. Either the Boys or ER localization scheme can be used to compute the mixing angles for constructing diabatic states. For all calculations shown here we used the Q-Chem 4.0 [23] code and employed the 6-31G(d)** basis set in order to compare our results against other theoretical results in Ref. [21].

2.3 ENERGY TRANSFER RATES IN DONOR-BRIDGE-ACCEPTOR SYSTEMS

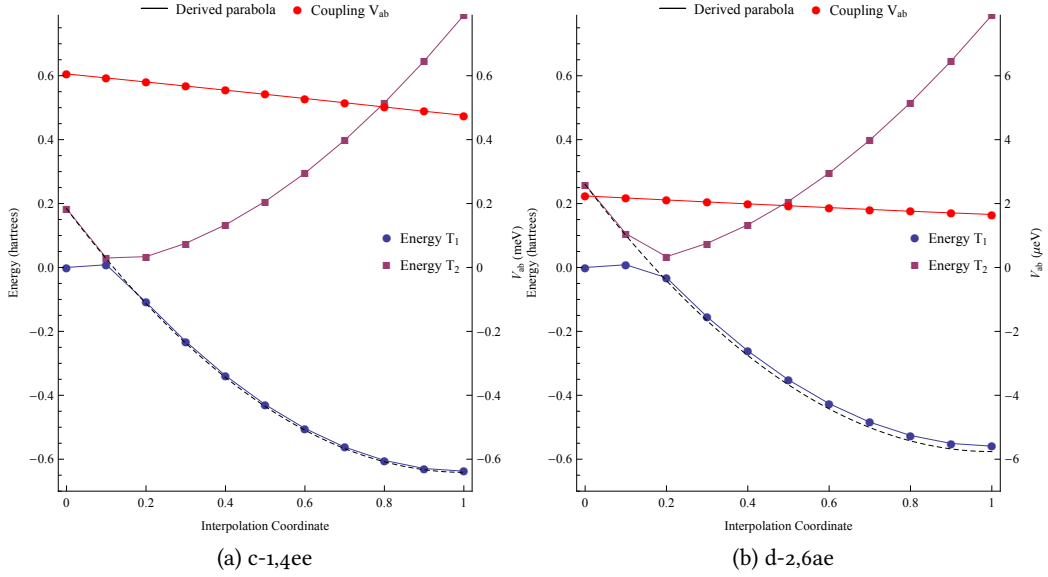


Figure 3.: Adiabatic energy curves and off-diagonal couplings computed along an interpolation coordinate between the $D^* - B - A$ and $D - B - A^*$ equilibrium geometries. V_{ab} is the off-diagonal coupling at each point along this coordinate.

We benchmark our approach against a series of donor-bridge-acceptor molecules studied by Closs [24–26]. These cases are significant in that they provided a crucial verification of the Marcus inverted regime. Table 1 and Fig. 4 summarize our results. In addition, we give the diabatic coupling V_{ab} , reorganization energy λ , and driving force $\Delta\epsilon$ computed using the Edmiston-Reudenberg (ER) localization method.

In general, our results and those in Ref. [21] agree with each other well and both are comparable to the experimental results which report an estimated error of 10-20% in the rate for each case presented here. Furthermore, all theoretical values were computed in the absence of solvent environment, whereas the experiments were all performed in benzene solvent at a standard temperature. However, there is considerable disagreement between the experimental and theoretical results for the d-2,6ea and methyl (M) bridged cases. For the d-2,6ea bridge, our results are similar to the Marcus theory rates given in Ref. [21]. In this case, the ER localization gives a small diabatic coupling and

Bridge	Structure	Rates (s^{-1})				Marcus theory parameters		
		Expt.	Marcus Theory	This work	Ref. [21]	λ (eV)	$\Delta\epsilon$ (eV)	V_{ab} (μeV)
c-1,3ea		3.3E9	3.9E9	2.2E9	0.823	-0.612	470.1	
c-1,3ee		7.7E9	2.1E10	2.8E10	0.810	-0.580	1687.3	
c-1,4ea		4.0E7	1.3E7	1.8E7	0.817	-0.604	43.20	
c-1,4ee		1.3E9	3.9E9	3.6E9	0.826	-0.642	605.8	
d-2,6ae		1.3E5	1.0E4	4.7E4	0.836	-0.577	2.239	
d-2,6ea		7.0E5	3.9E4	5.8E4	0.821	-0.609	2.414	
d-2,6ee		3.1E6	5.0E6	4.8E6	0.810	-0.581	22.12	
d-2,7ae		1.1E7	2.8E7	3.0E7	0.826	-0.605	55.16	
d-2,7ea		1.5E7	1.8E7	4.3E7	0.817	-0.605	65.85	
d-2,7ee		9.1E7	3.5E8	3.4E8	0.831	-0.648	185.1	
M		5.0E10	n.r.	1.2E9	0.896	-0.636	357.0	

Table 1.: Comparison of triplet-triplet energy transfer rates obtained from our approach, Marcus rates are from Ref. [21] and experimental rates from Refs. [24, 26]. The experimental error is estimated to be 20% in each case studied here. The V_{ab} are the diabatic couplings obtained using Edmiston-Ruedenberg diabatization. In each case, D = 4-benzophenonyl and A = 2-naphthyl. n.r. = Not Reported.

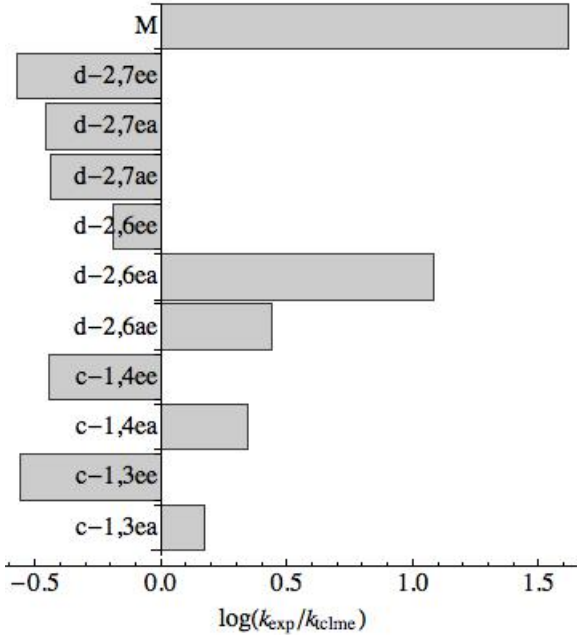


Figure 4.: Comparison between predicted (TCLME) rate constants and the experimental rates from Ref. [18]. With exception of the methyl and D-2,6-ea bridged cases, the TCLME results are in good agreement with the experimental results.

it was difficult to obtain converged localized states. In the case of the methyl-bridge, there is a significant change in the geometry between donor and acceptor states. As a result, the potential surfaces are no longer parabolic and the Condon approximation breaks down [21].

As an illustrative example of our approach, we consider the first few collective modes for the c-1,4ee and d-2,5ae cases. In Fig. 5 we show the projection of the primary coupling mode onto the coordinate frame of each molecule. The vectors indicate the direction of the electron-phonon coupling vectors projected onto the Cartesian displacement vectors of the individual atoms. In each case, the primary coupling mode involves the A_g in plane C=C stretching motions of the naphthalene donor and the in-plane A_1 ring-squeezing motions of the benzaldehyde acceptor. It is interesting to note that if we were to approximate naphthalene as a D_{2h} molecule, and benzaldehyde as a C_{2v} molecule, taking the aldehyde as local site, the primary coupling modes always correspond

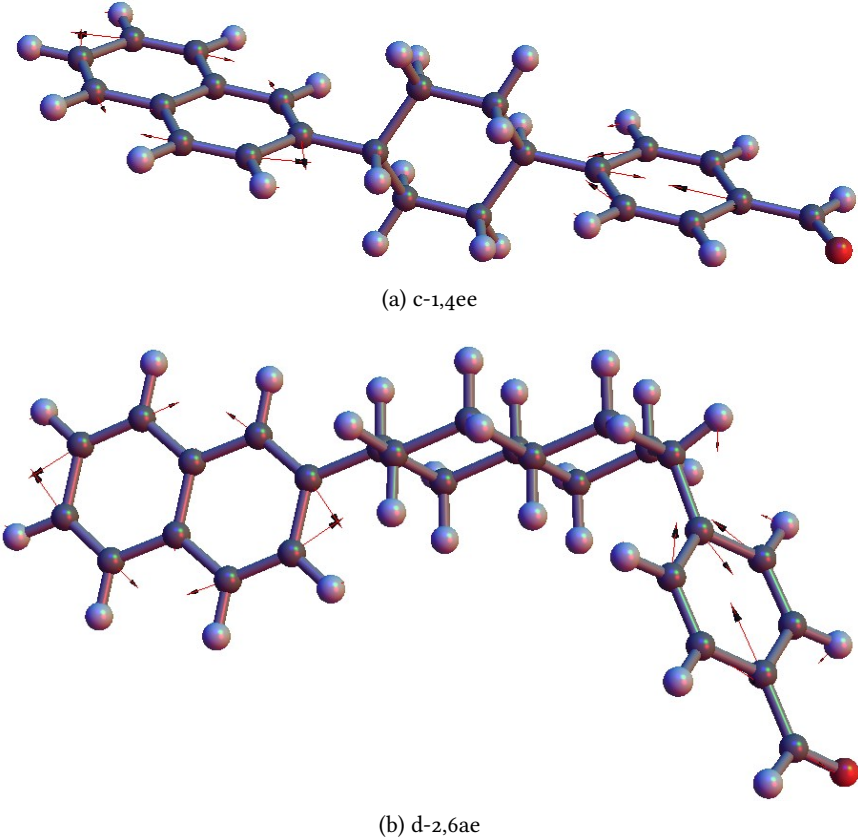


Figure 5.: Primary coupling modes for (a) c-1,4ee and (b) d-2,6ae projected onto the atomic displacement coordinates.

to the totally symmetric irreducible representations on moieties. Further analysis of symmetry reveals interesting details of the reactions, which are discussed in next chapter.

In order to substantiate our claim that the reduced modes generated by the iterative procedure capture the most important electron-phonon couplings, we consider the convergence of the electron-phonon autocorrelation function used to compute the golden-rule rate constants

$$C(t) = \langle \hat{V}_{nm}(t) \hat{V}_{nm}(0) \rangle \quad (2.1)$$

with respect to the number of reduced modes. We calculate this term exactly using all N vibrational modes of the molecule and compare to the results obtained using a subset of modes. Correlation function is used to compute transfer rate. Such comparison of correlations is very high standard test of the method. If we get good agreement, it means the reduced modes are a good representation of nuclear motions involved in transfer; even we do not get perfect correlation function, the rate constants calculated may also agree well, which is still a success.

In Fig. 6 we examine the convergence of $C(t)$ with respect to number of reduced modes for the c-1,4ee and d-2,6ae cases. In both cases, only a handful of reduced modes (4 for c-1,4ee and 15 for d-2,6ae) is needed to accurately track the correlation function for the first 10 fs. For comparison, d-2,6ae has 162 normal modes and c-1,4ee has 132 normal modes. For the primary mode approximation, the recursions appear every 23 fs and are suppressed by the addition of more reduced modes to the calculation. The 23 fs recursion time corresponds to the period of the single reduced mode: $\omega_1 = 0.18\text{eV}$ (1450 cm^{-1}). For the d-2,6ae case, including 15 modes is sufficient to fully suppress the recursion time to beyond 100 fs. For purposes of computing golden rule rate constants, the Markov limit is reached when $C(t) \rightarrow 0$. For the cases at hand, this is well before the first recursion seen in Fig. 6.

While it is surprising that only a few reduced modes are needed to converge the coupling correlation function, only a single mode is necessary to accurately compute the golden-rule rate constant. In Fig. 7 we compare the exact rate constant (using all modes) and rate constants computed using only the first mode generated by the Lanczos iterations. In the first case represented by the blue points, we approximate the renormalized energy as

$$\lambda_{nm} \approx \frac{g_1^2}{\omega_1}$$

where g_1 and ω_1 are the coupling and frequency of the first reduced mode. This simple approximation does a superb job compared to the numerically exact rate obtained using all modes and all couplings.

2.3 ENERGY TRANSFER RATES IN DONOR-BRIDGE-ACCEPTOR SYSTEMS

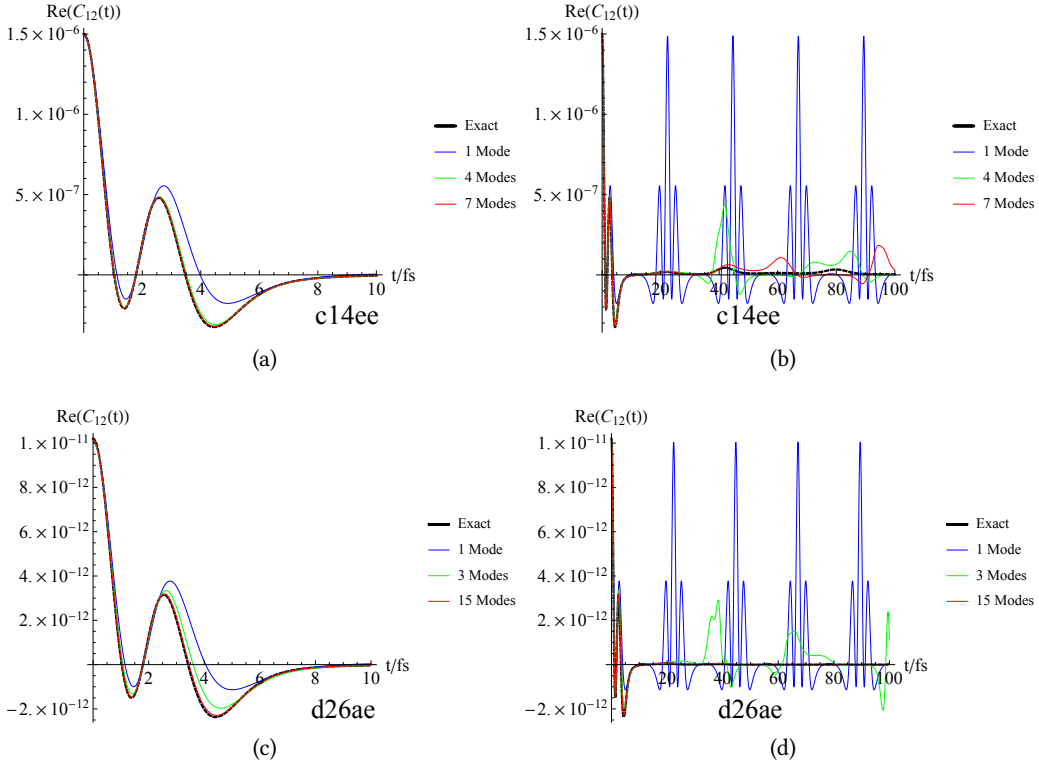


Figure 6.: Convergence of the electronic coupling autocorrelation function (Eq. 2.1) with respect to number of reduced modes.

On average, the error between the exact and approximate rate is 2% over the entire series of model donor-bridge-acceptor systems considered. The red points represent rates computed using the first reduced mode, but use the exact renormalized energy. Here, the agreement is almost perfect for the two fastest rates corresponding to d-2,6ae and d-2,6ea. However, on average this approximation is off by a factor of 3 compared to the exact rate. For the methyl-bridged case, the rate is off by a factor of 8.. This implies that the first reduced mode indeed captures the majority of the electron-phonon coupling and provides a unique description of the Marcus reaction coordinate.

In Table 2 we tabulate the frequencies and electron-phonon coupling constant for the first reduced mode for each test case. Uniformly, these modes correspond to ring breathing motions on the donor and acceptor as illustrated in Fig. 5. As seen in this figure, the coupling mode does not involve

2.4 DISCUSSION

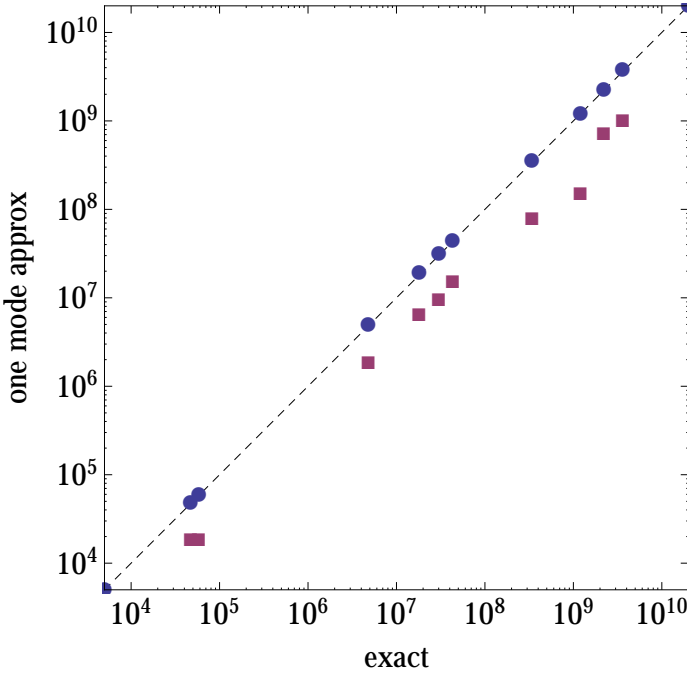


Figure 7.: Comparison between exact rate constant and its primary mode approximation. The blue points correspond to rates computed using only the primary mode and the renormalized energy for only that mode. The red points use the primary mode and the exact renormalized energies.

normal modes localized on the bridge species. Moreover, the magnitude of the electronic coupling carried by this mode is uniformly around 0.37 eV and independent of the bridge. No single normal mode captures all of the electronic coupling. This is evidenced by the fact that the magnitude of the electronic coupling carried by the first reduced mode is over twice that of the largest coupling along a single normal mode.

2.4 DISCUSSION

We present here a new approach for computing intramolecular energy and charge transfer rates by combining a time-convolutionless master equation approach for state to state population transfer as parameterized by a rigorous quantum chemical approach. The approach is robust over a wide range

2.4 DISCUSSION

bridge	ω_1 (eV)	$ g_1 $ (eV)	$ g_{max} $ (eV)
c-1,3ea	0.184	0.367	0.159
c-1,3ee	0.185	0.365	0.162
c-1,4ea	0.185	0.367	0.166
c-1,4ee	0.185	0.370	0.171
d-2,6ae	0.185	0.367	0.159
d-2,6ea	0.185	0.367	0.142
d-2,6ee	0.185	0.365	0.143
d-2,7ae	0.184	0.366	0.165
d-2,7ea	0.185	0.367	0.142
d-2,7ee	0.185	0.370	0.149
M	0.184	0.366	0.160

Table 2.: Frequencies and dimensionless electron-phonon couplings for the primary mode. The last column gives the absolute value of the largest coupling constant within the normal mode basis.

of model systems and generally gives good agreement compared to experimental rates and Marcus theory rates. Only in cases where the parabolic approximation to the diabatic potentials breaks down or when the ER localization method fails to converge is the agreement with the experimental rates less than satisfactory.

A crucial part of our analysis is the identification of a subset of collective modes that contain the electron-phonon couplings. Moreover, we show that there exists a unique mode—the “primary mode”, determined via an iterative approach, along which the off-diagonal electron-phonon coupling is maximized. Using only the primary mode mode as input to our golden-rule rate expression, we obtain excellent agreement (to within 2% on average over all of the donor-bridge-acceptor systems studied here) when compared to an exact evaluation using all normal modes. One can visualize the primary mode by projecting it on to the nuclear displacement vectors and gain insight into the coupled electronic/nuclear motions that underlie an electronic transition. Our analysis also suggests that the primary mode resembles certain irreducible representations of the donor and acceptor moieties. This connection is further explored in next chapter.

3

PRIMARY MODE AND ITS RELATION TO TRANSFER DYNAMICS

3.1 INTRODUCTION

In this chapter we analyze the symmetry of PLMs (see Fig. 5) in model donor-bridge-acceptor systems as projected onto the local vibrational modes of the donor (benzaldehyde) and acceptor (naphthalene) moieties. By constructing the local modes from the dominant normal modes in the projection, one can deduce a relation between the PLMs, fragment modes, and normal modes for the entire molecule.

In the next two sections, we discuss the symmetry of PLMs and their relation to a linear coordinate linking the initial/donor geometry to the final/acceptor geometry of the molecule. We first project the PLMs onto the normal modes of both the donor or acceptor moieties and onto entire molecules (donor-bridge-acceptor). Using these reduced PLMs we compute rate constants and compare to the numerically exact results obtained using the full modes. Then we do a similar set of projections using simply the geometric change from initial to final configurations to explore the relation between the PLMs and geometry.

3.2 SYMMETRY OF THE PRIMARY LANCZOS MODES

Fig. 8 shows the projection of the PLMs onto the normal modes of donor and acceptor moieties in molecules of c-1,4ee and d-2,6ae, respectively. In each case, we label the dominant contributions by

o Part of this chapter has been published in Xunmo Yang and E. R. Bittner, Computing Intramolecular Charge and Energy Transfer Rates Using Optimal Modes. *The Journal of Chemical Physics* **142**, 244114 (2015)

3.2 SYMMETRY OF THE PRIMARY LANCZOS MODES

the irreducible representations (IR) of the moiety. There are 4 sets of normal modes used as basis in projections. Two are the normal modes of benzaldehyde and two of naphthalene. They are generated as follows: first, we take the coordinates of benzaldehyde and naphthalene from the equilibrium geometry of c-1,4ee and d-2,6ae, and add necessary hydrogens. In theory, naphthalene has D_{2h} symmetry. However, by taking coordinates directly from the D-B-A molecules, the geometry of naphthalene is distorted slightly by the bridge and acceptor moieties, and its point group reduces to C_1 . We want the naphthalene to have high symmetry, so we can use the irreducible representations of D_{2h} to classify its normal modes. As the result, we use GaussView 5 to enforce D_{2h} symmetry on naphthalene. For benzaldehyde, we leave the coordinates unchanged, as there is no obvious way to increase the symmetry for benzaldehyde. Finally we run frequency computations for all 4 sets of coordinates.

If one treats the aldehyde group as a local site, one can classify the ring-motions of benzaldehyde in terms of the C_{2v} irreducible representations. As a result, the assigned irreducible representations are exact for naphthalene but approximate for benzaldehyde. We then assign a weight to each mode viz.

$$w_i = \frac{\left\langle \vec{M}_i | \overrightarrow{PLM} \right\rangle^2}{\sqrt{\sum_i \left\langle \vec{M}_i | \overrightarrow{PLM} \right\rangle^2}}$$

where \vec{M}_i is the displacement vector of the i th normal mode, and \overrightarrow{PLM} is the displacement vector of the PLM on the corresponding moiety. For example, for naphthalene, the \overrightarrow{PLM} are the vectors in Fig. 5, with only the atoms of naphthalene kept. The symmetrization of naphthalene introduces a subtle problem. The \overrightarrow{PLM} is based on the distorted geometry of naphthalene in the D-B-A molecule, while \vec{M}_i is computed on the geometry of symmetrized naphthalene. Two geometries differ slightly, so $\left\langle \vec{M}_i | \overrightarrow{PLM} \right\rangle$ depends on how we orient them. We choose to orient the original and symmetrized frames by first aligning the center of masses and then minimize the RMS displacement between atoms. This is arbitrary. Fortunately, two geometries are really similar, so we expect the choice of

3.2 SYMMETRY OF THE PRIMARY LANCZOS MODES

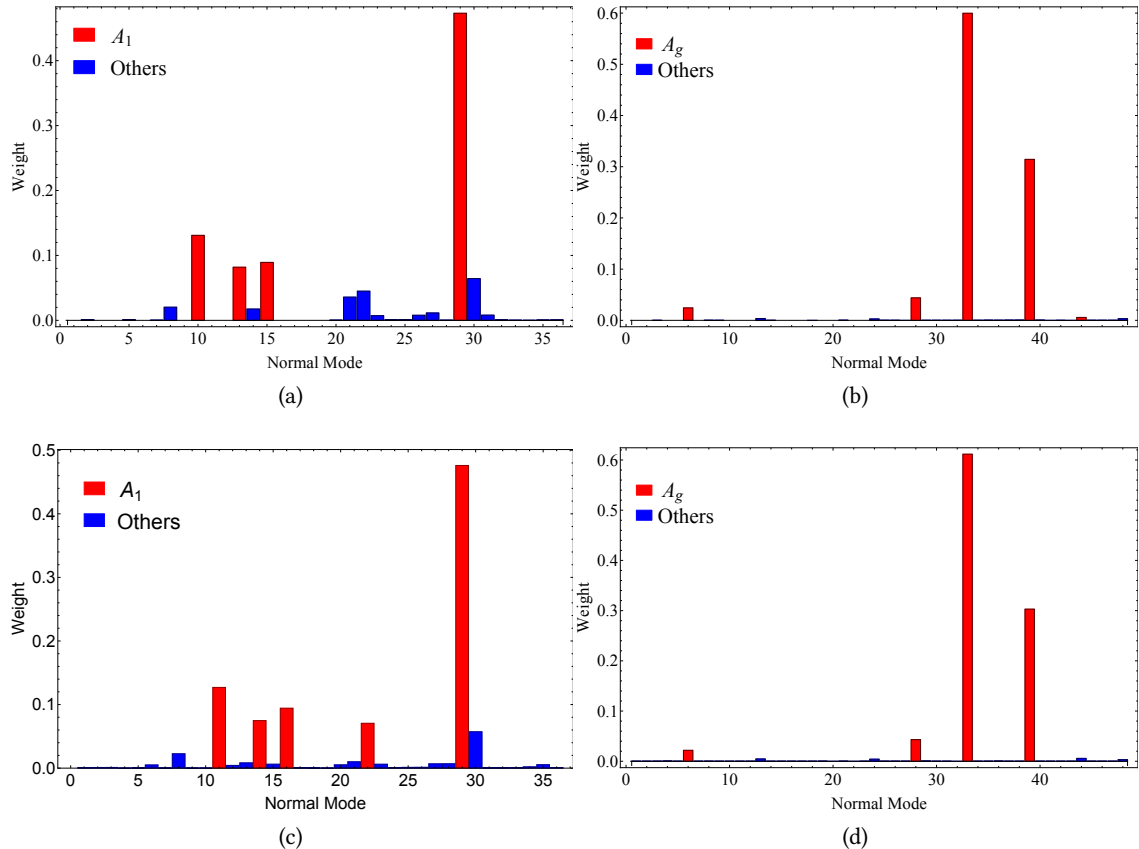


Figure 8.: Projection of PLMs onto (a) benzaldehyde in c-1,4ee (b) symmetrized naphthalene in c-1,4ee, (c) benzaldehyde in d-2,6ae and (d) symmetrized naphthalene in d-2,6ae. The normal modes are listed from low to high frequency and the irreducible representations of the dominant modes are color-coded. The assigned IRs for naphthalene are exact whereas the IRs are only approximate for benzaldehyde.

3.2 SYMMETRY OF THE PRIMARY LANCZOS MODES

orientation, as long as it is not ridiculous, is acceptable. By analyzing the projections it becomes clear that in all cases, the dominant components belong to totally symmetric A_g or A_1 irreducible representations, in agreement with the intuitive observations from Fig. 5.

This behavior is not unique for the naphthyl-bridge-benzaldehyde system. To see this, we repeated the analysis by replacing naphthalene with various acceptor groups, as shown in Fig. 9. Fig. 9 also shows the corresponding PLMs and correlation functions. For both molecules, 4 projected modes are enough to reproduce the exact (all modes) correlation function up to 10 fs. It indicates that the projection scheme provides an accurate description of the electronic coupling in these cases as well. Moreover, the PLMs in Fig. 9 are qualitatively similar to those in Fig. 5, where the acceptor is naphthalene. The displacements vectors on the benzaldehyde moiety in all 4 molecules are almost identical, and the displacements vectors on the naphthalene, phenyl and anthracene moieties all belong to totally symmetric irreducible representations.

It is not a coincidence that the PLMs belong to the totally symmetric irreducible representation of the isolated donor and acceptor moieties. This connection can be understood by analyzing the corresponding changes in the electron density that accompany the transition. For example, the PLM on the naphthalene part shown in Fig. 5 largely corresponds to a symmetric ring-stretching mode, involving carbons C₁ - C₂, C₃ - C₄, C₅ - C₆, and C₇ - C₈. During the exciton transfer, an electron is promoted from the naphthalene HOMO to the naphthalene LUMO (shown in Fig. 10) and one expects that changes in the bond lengths should reflect the changes in electronic population. For naphthalene, a HOMO → LUMO transition would decrease the π -bond order between C₁ - C₂, C₃ - C₄, C₅ - C₆, and C₇ - C₈. Similar statements can be made for the phenyl and anthracene systems. In next section, we examine the PLMs and bond-length changes that occur during an energy transfer event. We show that, in a more quantitative way, while the PLMs can be understood in terms of geometric changes in the molecule, the reverse is not true. It is not at all straightforward to determine the PLMs by taking the difference between the initial and final geometries of the molecule.

3.3 LOCALIZED PROPERTY OF THE PRIMARY LANCZOS MODE

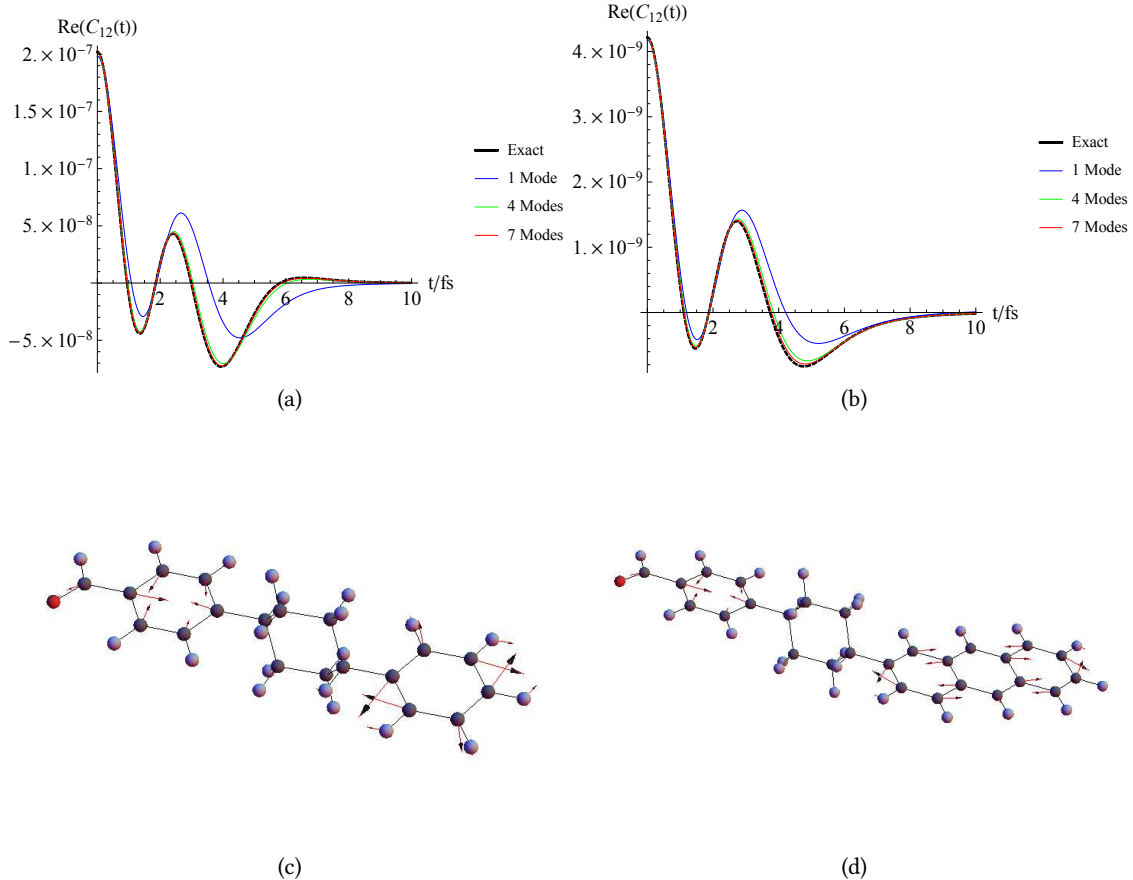
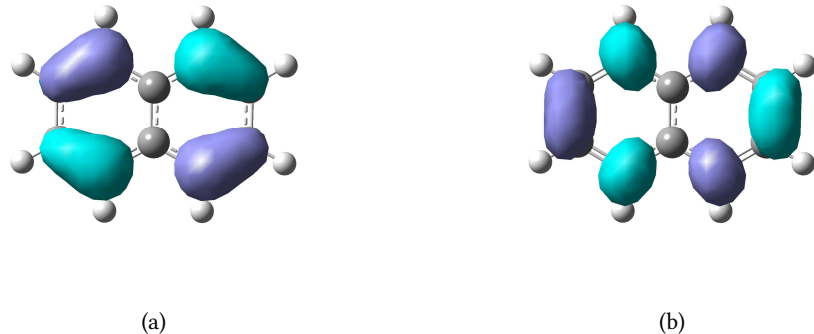


Figure 9.: The correlation functions of projected modes for c-1,4ee with the naphthalene moiety replaced by (a) phenyl ring and (b) anthracene, with their PLMs shown in (c) and (d).

3.3 LOCALIZED PROPERTY OF THE PRIMARY LANCZOS MODE

We have established that the primary Lanczos mode is more like the normal modes of the isolated donor and acceptor moieties, rather than of the entire molecule. The relation between the PLM and bond length change partially verifies our statement. In this section, we explore the localization in greater detail. First, we project the PLM onto the normal modes of entire molecule, which is shown in Fig. 11, as a comparison to Fig. 8, where the normal modes of the individual moieties are used. It is clear that on the basis of entire molecule, more modes are significantly involved. This is in contrast

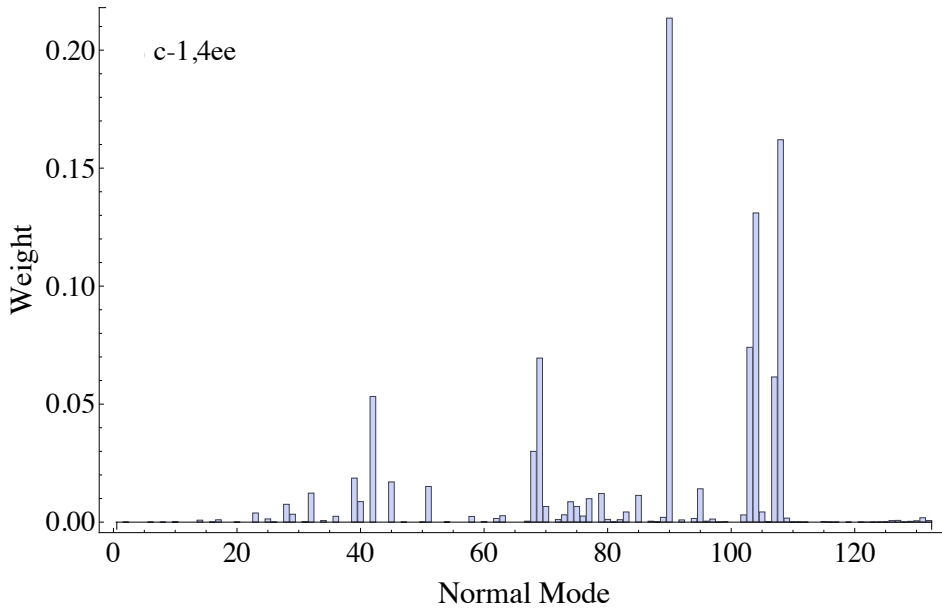
Figure 10.: The (a) (A_u) HOMO and (b) (B_{2g})LUMO of naphthalene.

to the projection of the PLM onto only the local modes of the isolated moieties, only a handful modes contribute. Since the PLM best captures the initial nuclear dynamics, its close relation with local sites reveals the fact that the exciton transfer here is more like a local excitation/de-excitation coupled by exchange interaction, in accordance with the Dexter mechanism [22].

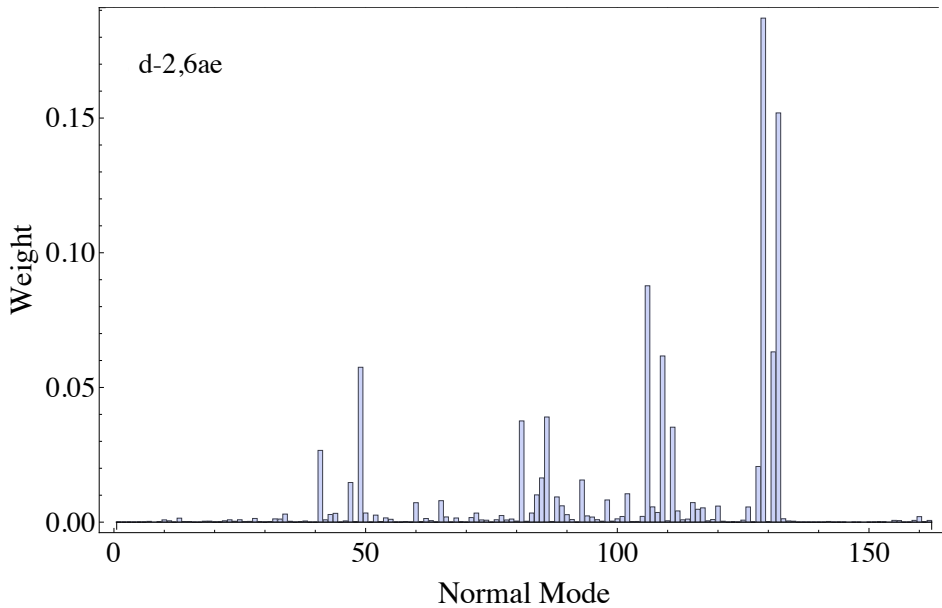
We do not include the bridge in the projections, because as showed in Fig. 5, very few motions involving the bridge contribute to the PLM. Thus, we anticipate that we can construct the PLM using only local modes on the donor and acceptor units. In the next section, we quantitatively verify this by using only dominant modes on the donor and acceptor to construct coupling modes.

However, before we can compare different ways to construct the Lanczos modes, we first need to address a subtle problem. In the previous section, we symmetrized the geometry of naphthalene for the convenience in assigning irreducible representations to the vibrational modes. However, for constructing the modes for the entire unit one needs to use the optimized rather than symmetrized geometry. In Fig. 12 we show the project of the PLM onto the modes for optimized naphthalene. The irreducible representations have been roughly assigned to the dominant modes. The projections are almost same to the ones on the symmetrized geometry, except a new B_{2u} mode is involved in c-1,4ee. However, it does not exist in d-2,6ae. The reason is that the most significant mode of c-1,4ee and d-2,6ae are slightly different. The corresponding displacement vectors are embedded

3.3 LOCALIZED PROPERTY OF THE PRIMARY LANCZOS MODE



(a)



(b)

Figure 11.: Projections of the PLM onto the normal modes of (a) $c-1,4ee$ and (b) $d-2,6ae$.

3.3 LOCALIZED PROPERTY OF THE PRIMARY LANCZOS MODE

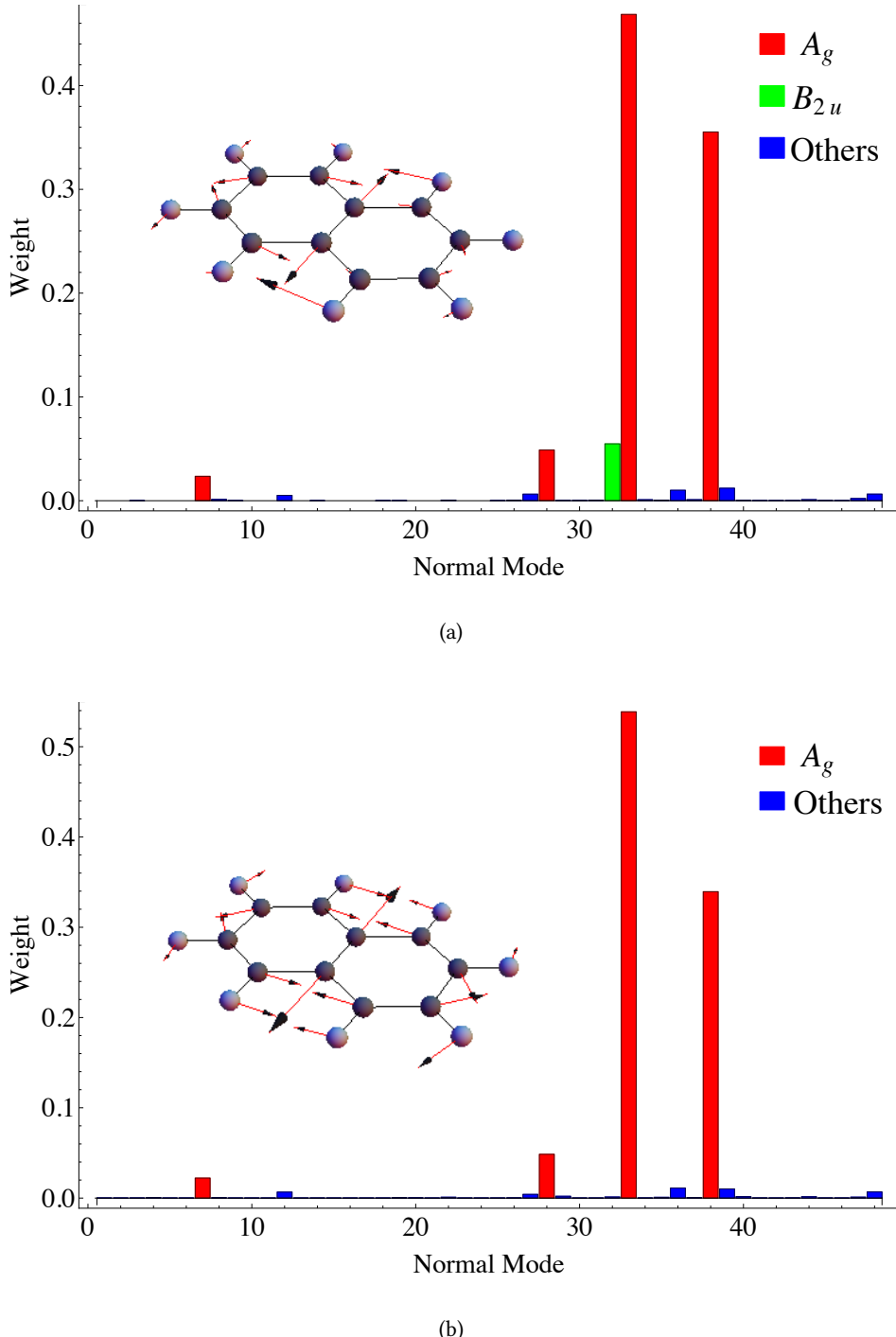


Figure 12.: Projection of PLMs onto unsymmetrized naphthalene for (a) c-1,4ee and (b) d-2,6ae. They are almost same to Fig. 8(b) and (d) except for a mode with B_{2u} symmetry in c-1,4ee. Embedded are the most significant modes, namely, the 33rd modes

3.3 LOCALIZED PROPERTY OF THE PRIMARY LANCZOS MODE

in Fig. 12. For c-1,4ee, the dominant mode is not an exact A_g mode, because carbons move in the way of A_g while hydrogens behave like B_{2u} . On the contrary, d-2,6ae has a mode more similar to A_g . As the result, in the projection of naphthalene in c-1,4ee, a B_{2u} mode is needed to correct the hydrogen motions.

To construct coupling modes, we collect a small number of modes on both naphthalene and benzaldehyde in the order of decreasing weights, then sum up the displacement vectors multiplied by their weights. We then bench-mark the quality of taking various different combinations of normal modes by computing the coupling auto-correlation function in Eq. 3 and comparing to the exact result obtained by including all modes. We denote these as $NxBy$ where x denotes the number of naphthalene local modes and y denotes the number of benzaldehyde local modes used in each case. NfBf denotes that *all* local modes are included. The correlation functions and rate constants derived from various combinations of normal modes are summarized in Fig. 13.

First, if we take all local modes from both moieties, (NfBf) the resulting approximated correlation function is indistinguishable from the exact correlation function. This verifies our observation that the bridge unit is not needed in constructing the PLM. In order to achieve adequate agreement with the exact correlation function, at least 10 of the strongest contributing local modes are needed from both the donor and acceptor units.

However, as seen on our previous work [27], the approximate correlation function does not need to give perfect agreement with the exact correlation function to produce an accurate transition rate constant (Eq. 4). To assess the accuracy of using different combinations of local modes, we calculate the transition rate constants for various combinations up to 10 modes on each moiety and compare to the exact rate. This data is summarized in the form of contour plots in Fig. 13(c,d). For the c-1,4ee case, there is an optimal “valley” whereby taking 3 modes from benzaldehyde and 4-6 modes from naphthalene produces an agreement with the exact result to within 5%. For the d-2,6ae case, fewer number of benzaldehyde modes than naphthalene modes are needed to give

3.3 LOCALIZED PROPERTY OF THE PRIMARY LANCZOS MODE

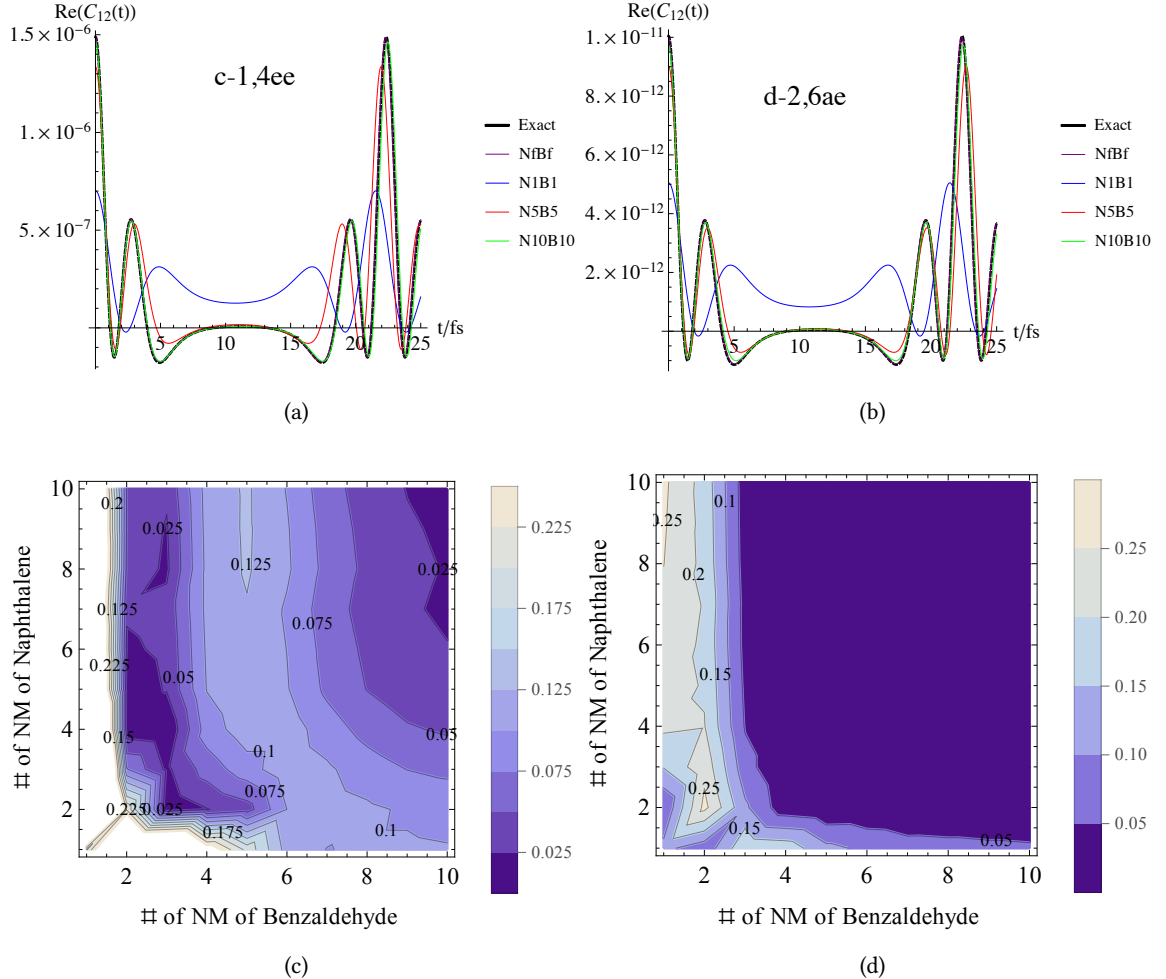


Figure 13.: Correlation functions for different combinations of normal modes are shown for (a) $c-1,4\text{ee}$ and (b) $d-2,6\text{ae}$. The “exact” ones refer are for the PLMs. “NfBf” is the mode made up from all normal modes of both the donor and acceptor sites. The designation “NxBy” indicates that the correlation function was constructed using x most significant normal modes on naphthalene and y most significant ones on benzaldehyde. Plots (c) and (d) show the relative error in rate constants calculated for various combinations of normal modes compared to the exact result of $c-1,4\text{ee}$ (c) and $d-2,6\text{ae}$ (d), respectively.

agreement to within 5% of the exact rate constant. This is easily anticipated since naphthalene is simply a larger molecule with more normal modes.

3.4 GEOMETRY CHANGE AND RELAXATION MODE

Table 3.: Approximated geometry using the PLM and the relaxation modes (RM) compared to acceptor states

Mode used	c-1,4ee-PLM	c-1,4ee-RM	d-2,6ae-PLM	d-2,6ae-RM
Max. bond length difference (Å)	0.034	0.160	0.039	0.283
Max. bond angle difference (rad)	0.053	0.075	0.057	0.135

3.4 GEOMETRY CHANGE AND RELAXATION MODE

We showed that the PLMs agree with bond length changes on the moieties. We next consider the relation between the PLM and geometry change accompanying the transition. First, we use the PLM to approximate geometry change by distorting the molecule along the PLM. The magnitude of the distortion is determined by minimizing the average bond length difference of the four bonds on naphthalene which stretch significantly in PLM, between the optimized and approximate geometries. In Table. 3 we list the differences between two geometries. Comparing the maximum difference of bond lengths and angles between the approximated and true final states, the differences are very small, so PLMs seem to give fairly good approximations of geometry changes.

However, this is only one side of the story and we need try to do this in reverse, *i. e.*, can we determine the PLM from simply geometric changes accompanying the transition? To see if this is possible, we can project the geometry change onto the normal modes of molecule and moieties respectively. The results for our two test cases are shown in Fig. 14 and 15.

When projected onto the whole molecule, we see that geometry change is mostly dominated by one very low frequency mode corresponding to an internal torsion of the entire donor-bridge-acceptor molecule. Compared to the PLMs in the same basis in Fig. 11 we see that PLMs have many more modes involved. However, if we compare the projections onto the moieties in Fig. 8 and 14, the geometry changes resemble PLMs well, except in the low frequency region. In essence, simply changing representation completely changes the implied dynamics.

3.4 GEOMETRY CHANGE AND RELAXATION MODE

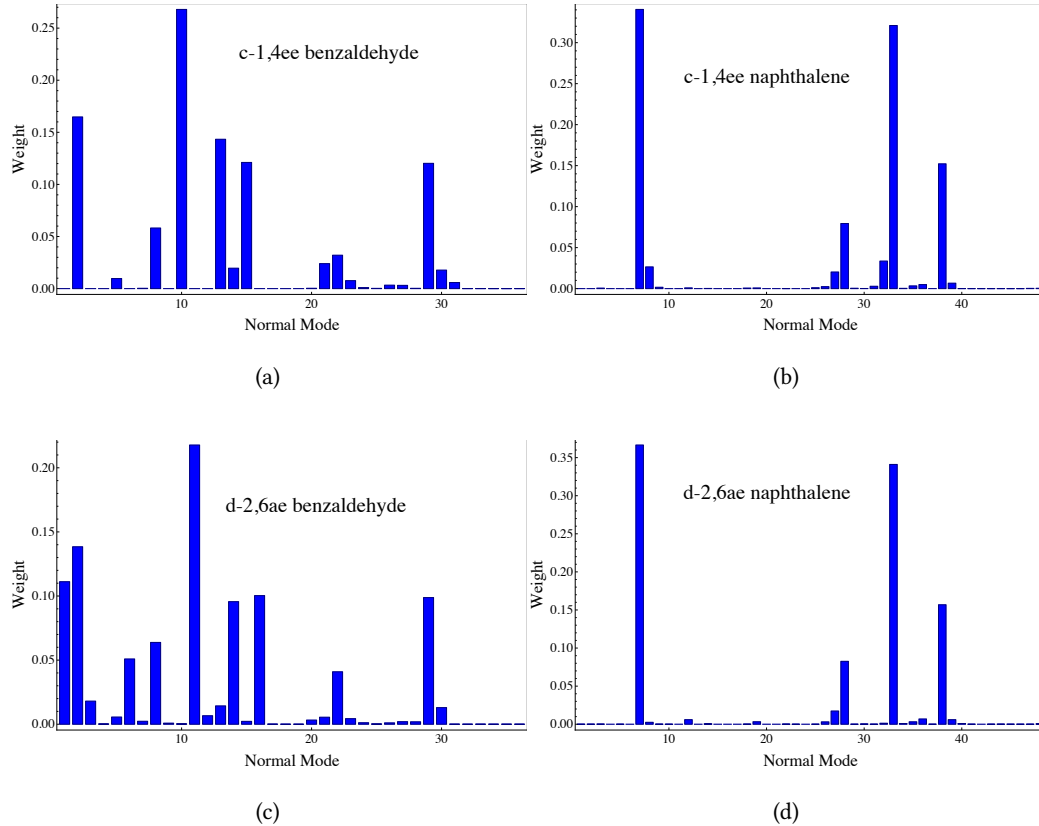


Figure 14.: Projections of the geometry change between initial and final states onto the normal modes of (a) benzaldehyde and (b) naphthalene sites in c-1,4ee, and d-2,6ae in (c) and (d). Except for some low frequency modes, they are similar to the projections of PLM.

The solution to this inconsistency is to distinguish between the two types of geometric changes. One is the internal changes within the moieties. These are well represented by the PLM. The other is the gross motion of the entire molecule, which we shall refer to as the “relaxation mode” (RM). This latter motion is not well represented by the PLM. These two kinds of motion correspond to two different steps that accompany the electronic transition. The internal motion primarily affects C=C bond lengths, and hence is strongly coupled to the π -electronic degrees of freedom, while gross motion of moieties corresponds to relaxation after exciton transfer has occurred. This is verified in Table 1, where we use the relaxation mode to approximate the final geometry. The procedure is

3.4 GEOMETRY CHANGE AND RELAXATION MODE

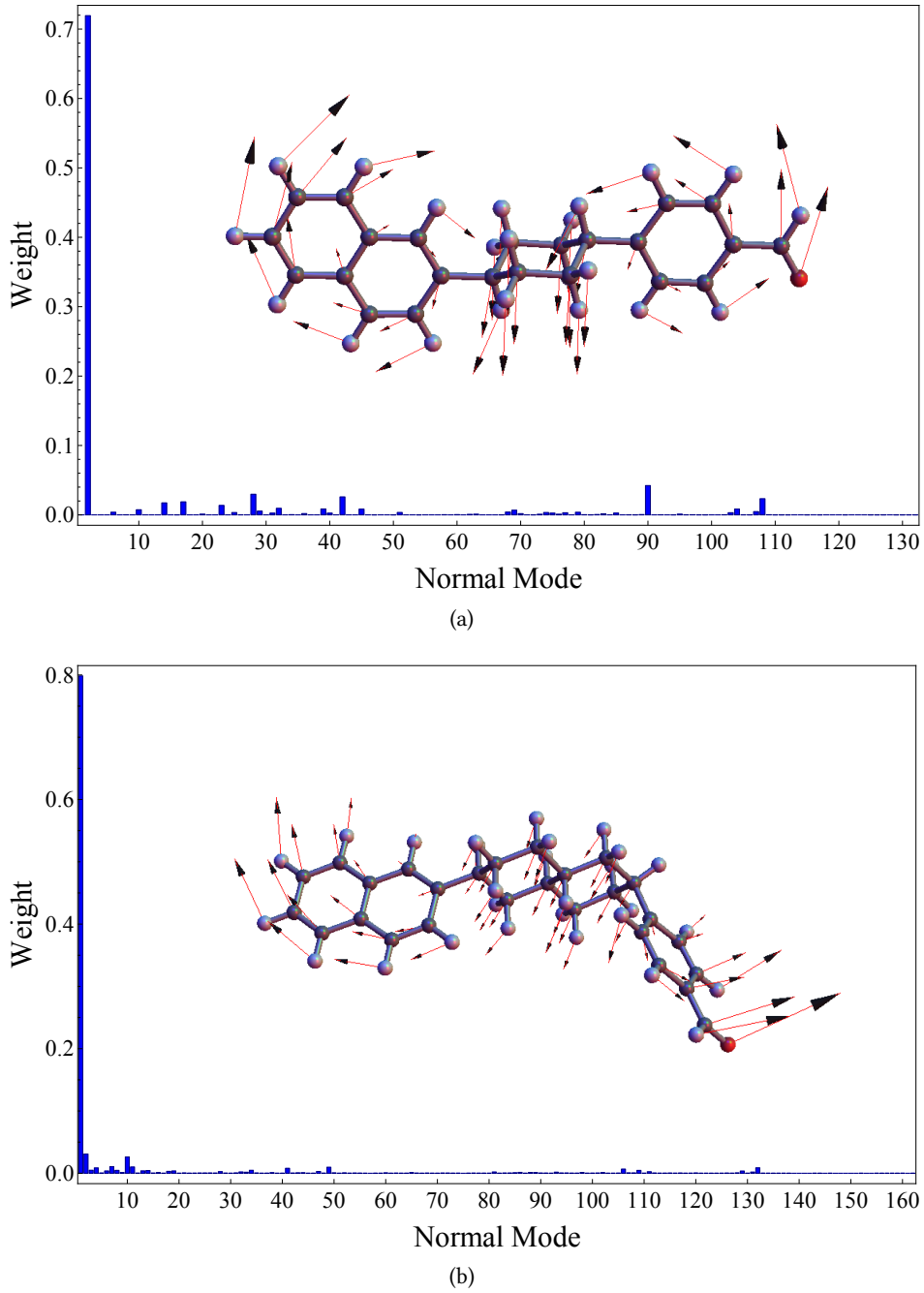


Figure 15.: Projections of the geometry change between initial and final states onto the normal modes of (a) c-1,4ee and (b) d-2,6ae. They are both dominated by single mode, the relaxation mode (RM), which is embedded.

3.5 DISCUSSION

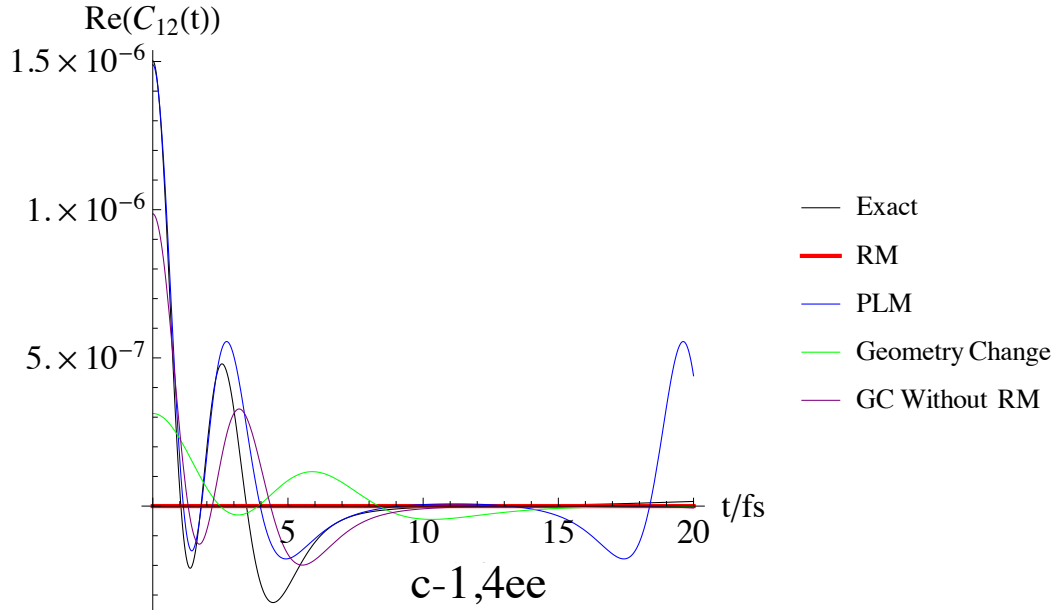
similar to that of PLM. Although RM is the dominant mode in the projection, it gives much worse approximated bond lengths and angles.

Since the PLM explains the short-time dynamics and can approximate the local geometry changes within the individual moieties very well, we anticipate that the PLMs facilitate the energy transfer step. To verify our prediction, we computed correlation functions of the electron/phonon coupling operators (Eq. 4) using different subsets of nuclear motions to estimate the couplings: PLM, RM, geometry change (GC), and geometry change with the RM component eliminated (GC-RM). The latter two correspond to taking the total geometric difference between the initial and final states of the molecule and projecting this onto normal modes, and to taking the geometric difference and subtracting off the relaxation mode. The various correlation functions and rate constants are summarized in Fig. 16. The exact results are obtained by using all normal modes and couplings. The PLM gives nearly perfect agreement to the exact calculation for both the time-correlation functions (Fig. 16) and the computed rates for both molecules considered (Fig. 17). The relaxation mode (RM) gives no contribution to the correlation function or the rate. Finally, using just the over-all geometric change (GC) gives a poor estimate of both the correlation function and the rate. GC-RM gives the initial transient dynamics in the correlation function and a reasonable approximation to the overall rate. However, the best agreement overall is obtained by using the PLM identified using the Lanczos search algorithm.

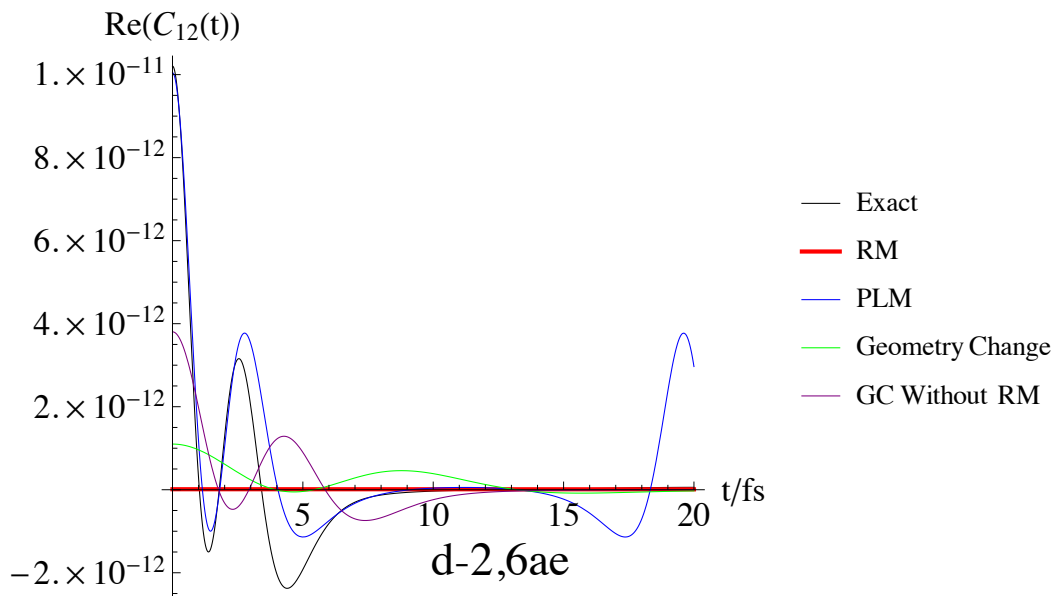
3.5 DISCUSSION

We presented here a further exploration of the classes of nuclear motions that accompany an electronic energy transition. We show that deeper insight can be gained by analyzing the primary modes and comparing them to both the geometric distortion of the molecule and to the electronic orbitals involved in the transition.

3.5 DISCUSSION



(a)



(b)

Figure 16.: Correlation functions of relaxation mode (RM), PLM, geometry change (GC), and geometry change with the RM component eliminated for (a) $c-1,4ee$ and (b) $d-2,6ae$. The exact rate is computed using the full set of normal modes.

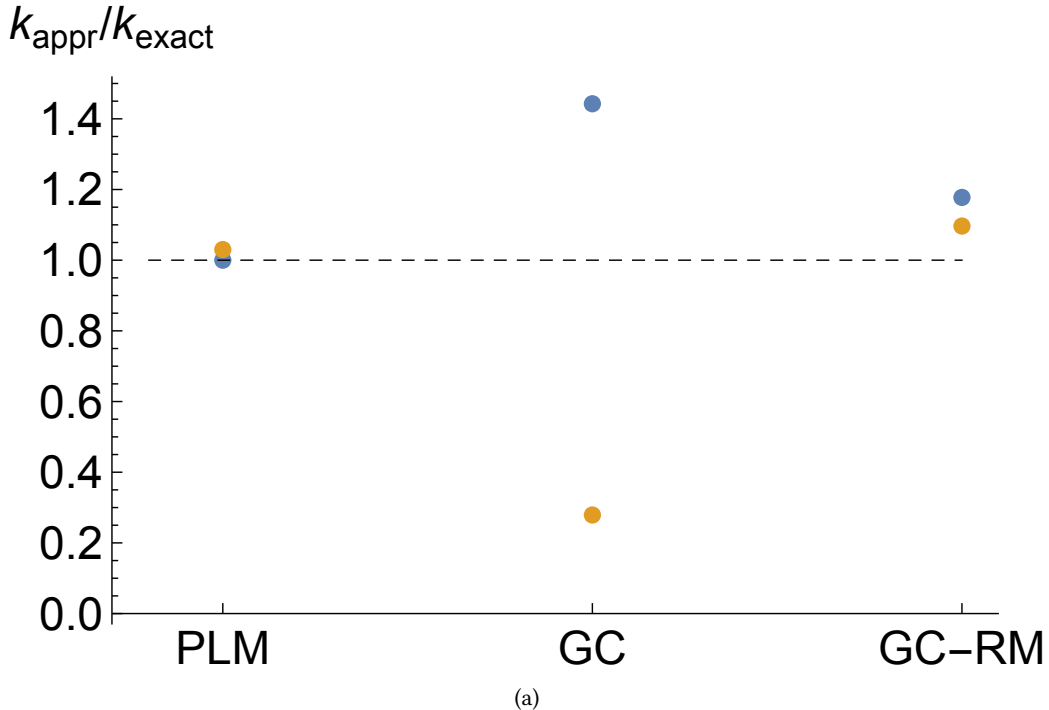


Figure 17.: Relative comparison of the rate constants computed using different sets of reduced modes. blue = c-1,4ee, gold = d-2,6ae.

Our results also suggest that the energy transfer process in these systems occurs in two distinct steps. The initial transfer from the donor to acceptor occurs in a fixed nuclear frame—as per the Condon principle. This fast transfer is facilitated by the PLM and involves excitations in the C=C bond lengths of donor and acceptor fragments in accordance with changes in the HOMO/LUMO populations of each fragment. After the exciton transfer, the entire molecule undergoes a slow but large geometric relaxation under the new electronic distribution.

Finally, we emphasize that the PLM approach and this analysis need not be limited to the energy transfer cases studied here. Combined with the time-convolutionless master equation approach, this provides a robust and efficient way for computing state-to-state transitions rates for a wide class of molecular systems.

4

APPLICATION ON MORE COMPLEX MOLECULES

4.1 INTRODUCTION

In previous chapters, we have benchmarked our approach against a well-known set of test cases. In this chapter we want to apply the method to an entirely new molecule. Recently, the Weinstein group at University of Sheffield reported upon a series of molecules, whose electron transfer (ET) pathways can be radically changed - even completely closed - by infrared light excitation of intramolecular vibrations [43–45]. The molecules are shown in Fig. 18. They are much larger than the molecules in previous chapters. Also, they contain heavy atoms, Pt, which makes the computation more difficult. Nevertheless, there is no difficulty in principle preventing us from applying our method to these molecules. They seem to be good candidates to further test our model.

In this chapter, we first briefly review their experiment results and the theory of our approach. Then we compare rate constants and mode that significantly affects dynamics.

4.2 EXPERIMENT RESULTS

Weinstein *et al.* designed and investigated three donor–bridge–acceptor (DBA) molecular triads [43–45]: PTZ-CH₂-Ph-C≡C-Pt- C≡C-NAP, PTZ-Ph-C≡C-Pt- C≡C-NAP and OMe-PTZ-Ph-C≡C-Pt- C≡C-NAP (D = PTZ is phenothiazine and A = NAP is naphthalene-monoimide, see Fig. 18(a)). From

4.2 EXPERIMENT RESULTS

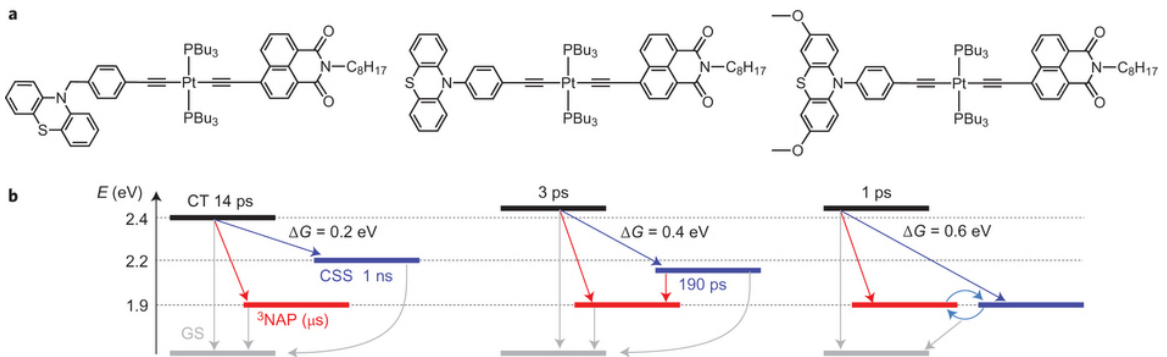


Figure 18.: a. Molecular structure of PTZ-CH₂-Pt-NAP, PTZ-Pt-NAP and OMe-PTZ-Pt-NAP, from left to right. b. Energy level diagrams for the ET process, with the lifetimes and the driving force (ΔG) of CT \rightarrow CSS transfer indicated. Adapted with permission from Ref. [44].

now on, they are further abbreviated as PTZ-CH₂-Pt-NAP, PTZ-Pt-NAP and OMe-PTZ-Pt-NAP, respectively.

All three molecules undergo similar ET processes after excitation, as illustrated in Fig. 18(b) and Fig. 19. Following UV excitation, molecules first jump to the triplet charge transfer (CT) manifold stemming from electron transfer from the Pt-acetylide center to the NAP acceptor. The transferred charge can undergo either further separation to form the full charge-separated state (CSS), or recombine to form a localized excitation, ³NAP. Both eventually decay to ground state. Weinstein *et al.* showed that if a judiciously chosen IR pump is applied to excite the C≡C bond after the initial UV excitation, the yield of intermediate states can be radically changed. For example, when a IR pump with frequency = 1,940 cm⁻¹ is applied to excite the C≡C in PTZ-CH₂-Pt-NAP, 1 ps after the UV pump, the yield of the CSS state decrease from 32% to 15%, while that of the ³NAP increases from 29% to 46%. The most striking observation is that when a 1,908 cm⁻¹ IR pulse is applied to PTZ-CH₂-Pt-NAP 2 ps after UV excitation, the CT \rightarrow CSS step is completely switched off, as illustrated in Fig. 19.

The molecules show different changes in yield because of the different donors. From PTZ-CH₂-Pt-NAP to PTZ-Pt-NAP, to OMe-PTZ-Pt-NAP, the donor strength increases, which enlarges the

4.2 EXPERIMENT RESULTS

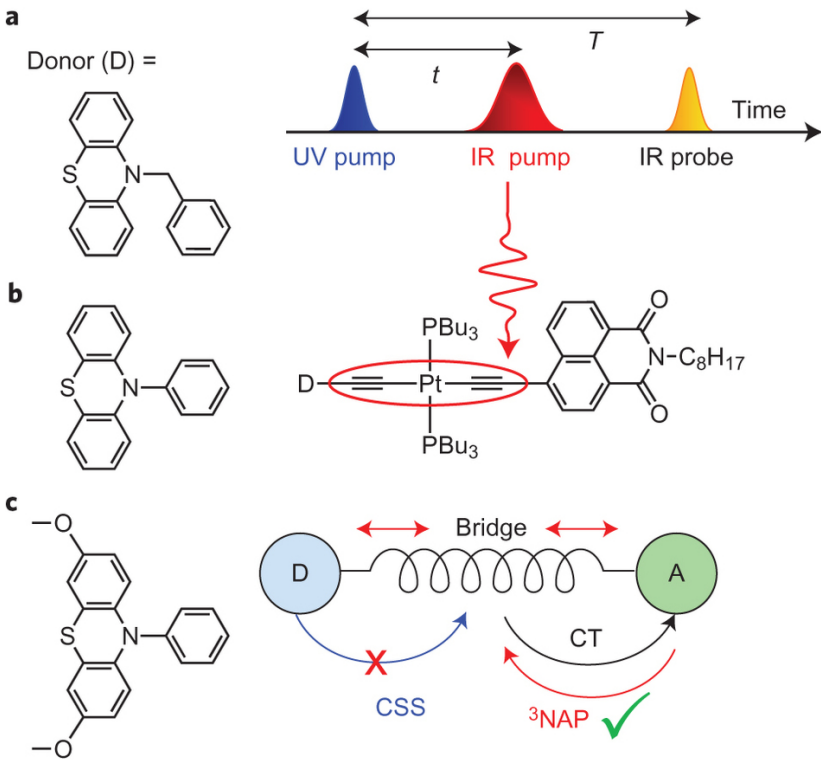


Figure 19.: The sketch of ET pathways. For PTZ-CH₂-Pt-NAP, the CT → CSS step can be fully suppressed by intermediate infrared excitation. Reprinted with permission from Ref. [44].

energy gap between CT and CSS states, as sketched in Fig. 18. The driving force (ΔG) of CT → CSS transfer increases from 0.2 eV in PTZ-CH₂-Pt-NAP, to 0.4 eV in PTZ-Pt-NAP, to 0.6 eV in OMe-PTZ-Pt-NAP. Large ΔG accelerates the CT decay and hence decreases the lifetime of CT state. Comparing PTZ-Pt-NAP and PTZ-CH₂-Pt-NAP, CT transfer to both charge separation and recombination slows down by a factor of ~5 (the lifetime of CT increases from 3.3 to 14 ps and CSS from 190 ps to 1 ns). By appending methoxy groups to the PTZ, the donor strength is increased, and reaction is accelerated. As the result, the lifetime of CT in OMe-PTZ-Pt-NAP is further reduced to 1 ps.

Weinstein proposes the effect of infrared control is caused by the fact that the distance between CT energy minimum and the intersection of CT and CSS potential energy surfaces is small. For all

4.2 EXPERIMENT RESULTS

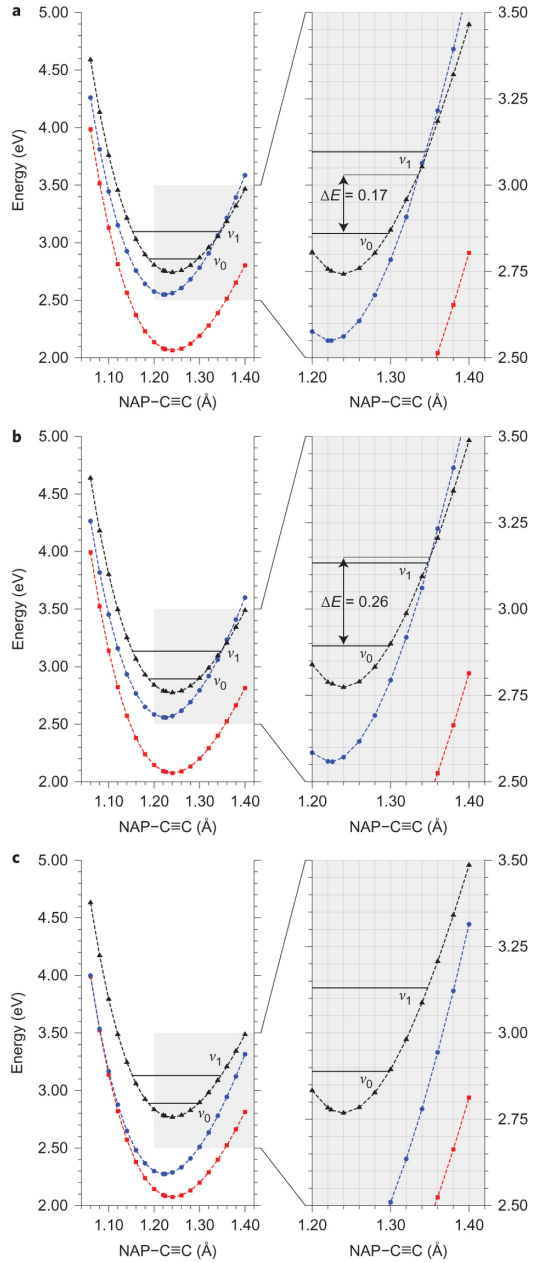


Figure 20.: Calculated energies of the CT (black) CSS (blue) and ³NAP (red) states along the NAP side C≡C coordinate in the ground state geometries of the molecules studied, in CH₂Cl₂. a, PTZ-CH₂-Pt-NAP. b, PTZ-Pt-NAP. c, OMe-PTZ-Pt-NAP. The first and second vibrational energy levels for the asymmetric C≡C stretch are shown for the CT state. The energy gaps from v_0 to the intersection between CT and CSS are shown in the insets. There is a clear trend concerning the energy gap: PTZ-CH₂-Pt-NAP < PTZ-Pt-NAP < OMe-PTZ-Pt-NAP, reflecting the trend experimentally observed in the efficiency of the infrared control effect. Reprinted with permission from Ref. [44].

4.3 THEORETICAL MODEL

three molecules, two PESs intersect where C≡C bond is slightly longer than the equilibrium length. When C≡C bond gets excited, it elongates and helps molecules to pass the intersection. If the energy gap between intersection and equilibrium geometry is much larger than C≡C vibrational energy, the dynamics is barely affected; if the energy gap is small, the vibrational excitation can radically change the dynamics. Fig. 20 shows the calculated PESs along the NAP side C≡C coordinate in the ground state geometries. Several observations can be drawn. First, they are quite parabolic, which suggest the parabolic assumption in our approach probably holds. Second, the geometry at the intersection of CT and CSS potential energy surfaces have longer C≡C bond than the equilibrium geometry. Third, PTZ-CH₂-Pt-NAP has the smallest energy difference between the intersection and the equilibrium geometry, agreeing to the explanation above.

4.3 THEORETICAL MODEL

In previous chapters, the diabatic coupling V_{ab} in Eq. 1.21, which determines the mixing angle θ in Eq. 1.20, is obtained via ER localization, while in this chapter it is computed via the generalized Mulliken-Hush (GMH) model [47, 48]. In principle, any diabatization approach can be used to parametrize Eq. 1.21. There are many diabatization approaches (for a review, see Ref. [12]), and can be classified into three categories. ER localization and GMH approach fall in one category [19, 20]. They do not seek diabatic states with zero derivative couplings, which are expensive to compute. Instead, they rely on physical intuition. GMH works well for linear or near-linear systems, but does not generalize to noncollinear system with more than two charge centers very well. ER localization can be seen as a extension of GMH which overcomes some drawbacks of GMH [20]. This time we obtain the frequency and optimized geometry from Weinstein group. They do the computation in Gaussian 09 [49], which does not support ER diabatization. Considering a typical calculation of such molecule takes months of CPU effort, we do not try to recompute it in Q-Chem. Instead, we turn to GMH. Fortunately, the molecule presented here is quite linear, and its charge centers are

4.4 RESULTS AND DISCUSSION

in the linear C≡C axis. As the result, GMH and ER localization approaches are expected to give similar results. The diabatic coupling given by GMH is

$$V_{ab} = \frac{(E_2 - E_1) |\mu_{12}|}{\sqrt{(\mu_1 - \mu_2)^2 + 4\mu_{12}^2}},$$

where $(E_2 - E_1)$ is the vertical excitation energy, μ_1 and μ_2 are the dipole moments of corresponding adiabatic states, and μ_{12} is the transition dipole moment between two states.

The molecules were optimized using DFT for ground state and TD-DFT for excited states in Gaussian 09. The molecules are simplified to speed up the computations. The P(Bu)₃ moieties and octyl chain of NAP are simplified to PH₃ and a methyl group, respectively. In all calculations, SDD pseudo potential and solvent model are used (see Appendix. D for the details of parameters). The transition dipole moments and electron/hole distributions surfaces are calculated using Multiwfn 3.3.8 [50].

4.4 RESULTS AND DISCUSSION

4.4.1 Rate Constant

The results presented here are for PTZ-Pt-NAP. The computation of other two molecules are in progress. We optimize and get two states of PTZ-Pt-NAP, the ³NAP and the lowest CT state. The energy diagram is sketched in Fig. 21, together with the electron/hole distribution plots. At both ³NAP or CT state geometries, the lowest state is the ³NAP, and there are two CT states above the CSS state. We can use parameters obtained at CT state geometry to compute transitions involving the CT state, and for ³NAP involved transitions, we use ³NAP geometry. Obviously, for the CT → ³NAP transition, we can use either geometry of CT or ³NAP.

4.4 RESULTS AND DISCUSSION

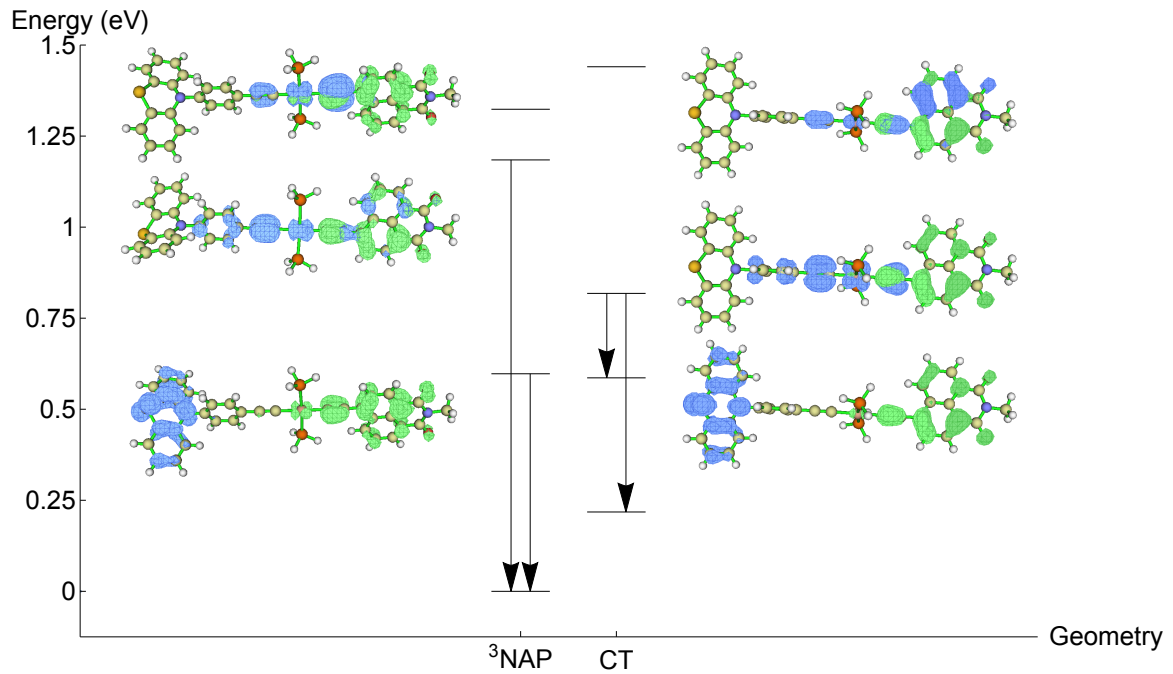


Figure 21.: The energy diagram of triplet states at ${}^3\text{NAP}$ and CT state geometries. The electron/hole distribution are shown as well (green for electron, blue for hole). The arrows indicate the transitions we calculate.

4.4 RESULTS AND DISCUSSION

The comparison between theoretical and experimental rate constants is summarized in Fig. 22. We calculate several sets of theoretical rates. First, we calculate the Marcus theory rates (Eq. 1.1). At the CT geometry, we get good agreement. However, at the ${}^3\text{NAP}$ geometry, the results are very poor. Second, we calculate the TCLME rates (Eq. 1.12). The results are still not satisfactory for the ${}^3\text{NAP}$ geometry. Nevertheless, TCLME is better than Marcus theory in all cases. We also calculate the TCLME rates with only the primary mode used. Still, they agree to the exact TCLME rates better at the CT geometry.

The failure of the ${}^3\text{NAP}$ geometry is especially obvious when we look at the $\text{CT} \rightarrow {}^3\text{NAP}$ transition. For this transition, we can calculate at either geometry. The TCLME rate constants at two geometries do not agree to each other. The results based on the CT geometry are in the same magnitude with experimental values, and the corresponding primary mode rates are similar to the exact ones. While the ${}^3\text{NAP}$ geometry performs poorly. In Section 4.4.3, we illustrate that the error is, at least partially, caused by the break down of Condon approximation, and according corrections may improve the results.

4.4.2 Primary Mode

In Fig. 22 we see that for the CT geometry, using only the primary mode is sufficient to get good rate constants. Fig. 23 shows the correlation functions of different numbers of projected modes for all four transitions. Again the CT geometry performs better. Its convergence is satisfactory. The primary mode always resembles the exact initial dynamics, especially for the $\text{CT} \rightarrow {}^3\text{NAP}$ transition, where the primary mode reproduces the dynamics almost exactly up to 9 fs. Though not perfectly, tens of projected modes are enough to reproduce the shape of exact correlation functions for CT geometry. On the contrary, it takes hundreds of modes to recover the correlation for ${}^3\text{NAP}$ (note that the degrees of freedom of PTZ-Pt-NAP is 201). Our previous studies [27] shows that perfect matching of correlation function is unnecessary for good rate constant. It is verified again

4.4 RESULTS AND DISCUSSION

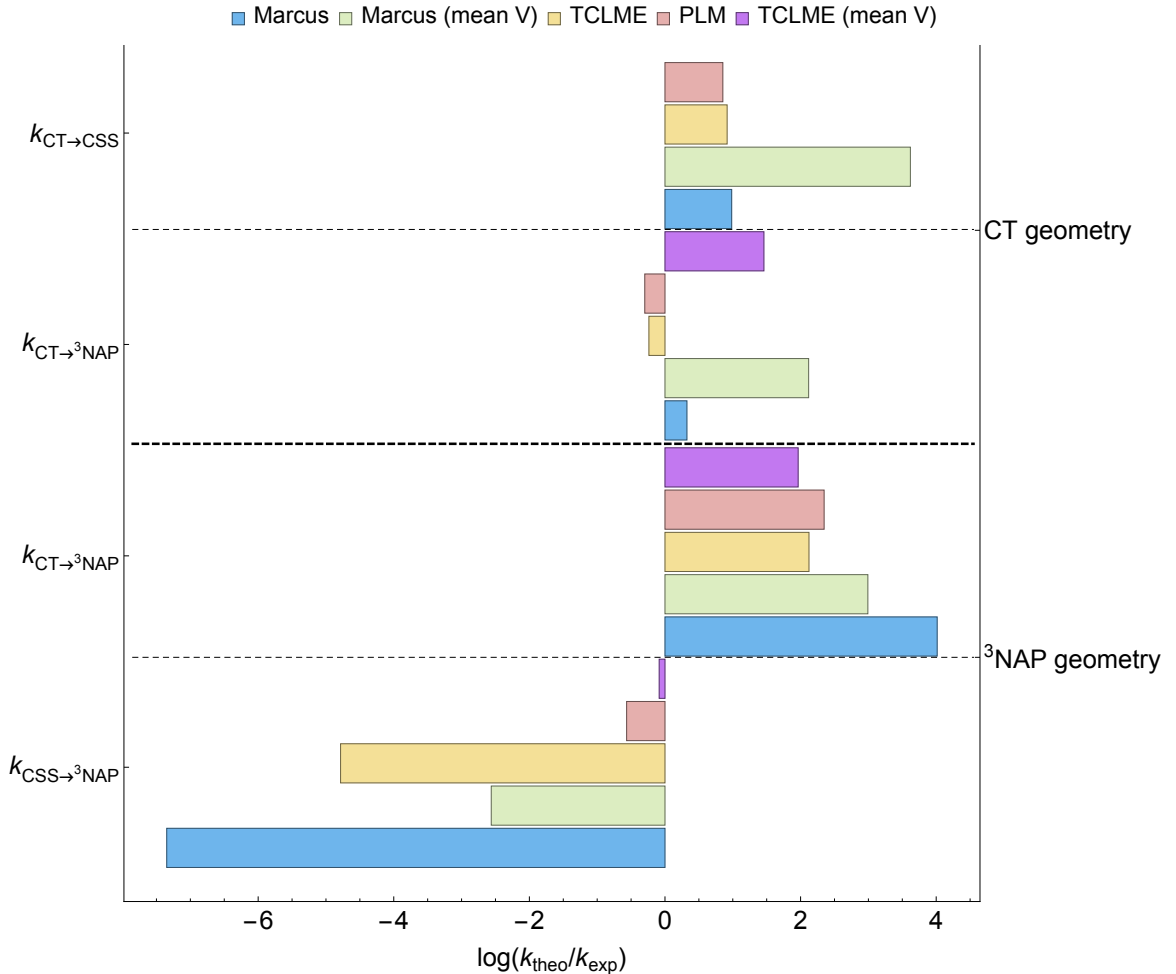


Figure 22.: Comparisons between theoretical rate constants and the experimental rates. Experimental rates are calculated as yield of product/lifetime of reactant, using values from Ref. [44]. The “Marcus” rates are calculated using Marcus theory with the diabatic couplings at according geometries. The “Marcus (mean V)” rates are calculated using mean diabatic couplings along the interpolated coordinate in Fig. 27. Similarly, the “TCLME” and “TCLME (mean V)” rates are calculated using the TCLME approach, with all normal modes used. The “PLM” rates are calculated using only the primary mode. Our approach performs better than Marcus theory. The CT geometry gives good “exact” results, its primary mode rates also agree well. While for the ${}^3\text{NAP}$ geometry, using mean value of diabatic couplings along the reaction coordinate significantly improves the performance.

4.4 RESULTS AND DISCUSSION

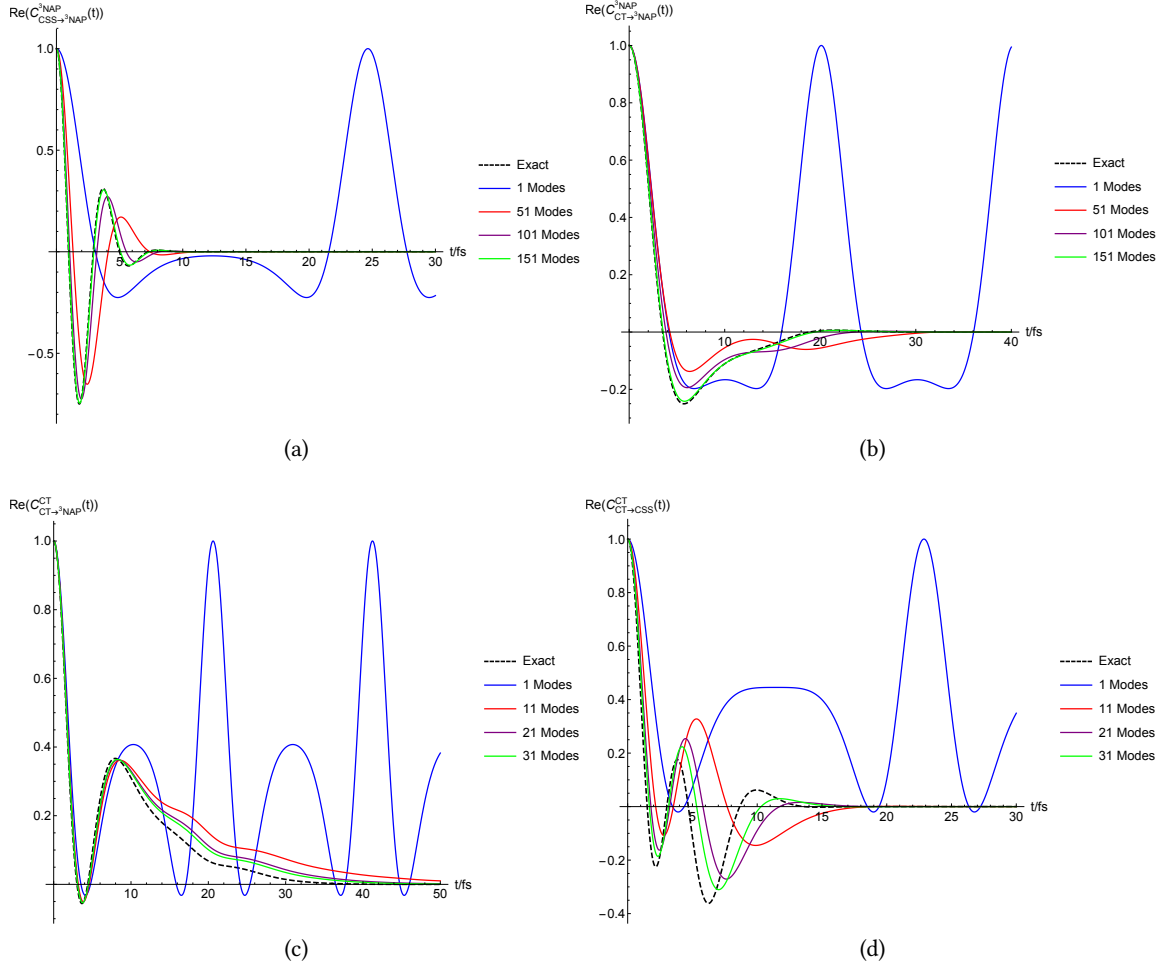


Figure 23.: Correlation functions of various numbers of projected modes, compared to exact correlation, for (a) CSS \rightarrow ${}^3\text{NAP}$ at ${}^3\text{NAP}$ geometry, (b) CT \rightarrow ${}^3\text{NAP}$ at ${}^3\text{NAP}$ geometry, (c) CT \rightarrow ${}^3\text{NAP}$ at CT geometry, and (d) CT \rightarrow CSS at CT geometry.

4.4 RESULTS AND DISCUSSION

here. The primary mode's correlation function at CT geometry does not match the exact correlation perfectly, but the rate it gives agrees well to the exact value, and experiments. Nevertheless, the better it resembles the shape of exact function, the better the rate constant it gives.

As experiments show that the excitation of C≡C bond radically affected the ET process, we expect the triple bond vibration to dominate the primary modes, at least for the CT state based calculations, since they achieve good agreement. Fig. 24 and 25 show the projection of primary modes onto the normal modes of corresponding state, *i. e.*, the primary modes calculated at CT geometry are projected onto the normal modes of the CT state, and those at ${}^3\text{NAP}$ are projected onto ${}^3\text{NAP}$'s normal modes. It turns out that all four primary modes involve obvious C≡C displacement, and it is verified by the projections. The projections of primary modes are dominated by 1 or 2 normal modes. In Fig. 24(a), it is the 174th normal mode (ordered by increasing frequency) that dominates; in Fig. 24(b), the 174th and 175th modes dominate. Similarly, 174th and 175th modes dominate in Fig. 25(a) and 175th mode in Fig. 25(b).

All these normal modes are C≡C stretching modes, as shown in Fig. 26. We suggest that the primary mode of CT → CSS transition (Fig. 25(b)) is the one involves C≡C vibration most. It has a component which has the largest weight, > 0.25 , in all four primary modes. And that component clearly dominates other normal modes. Experimentally, after the IR pump is applied, the CT → ${}^3\text{NAP}$ transition is relatively accelerated compared to the CT → CSS transition. By comparing the primary modes of the two transitions at CT geometry, we see that the primary mode of CT → ${}^3\text{NAP}$ transition is mainly antisymmetric stretching of two C≡C bonds, while that of CT → CSS transition is symmetric. As a result, the primary mode of CT → ${}^3\text{NAP}$ is more IR active than that of CT → CSS transition. It may explain why CT → ${}^3\text{NAP}$ transition is relatively accelerated with IR pump.

4.4 RESULTS AND DISCUSSION

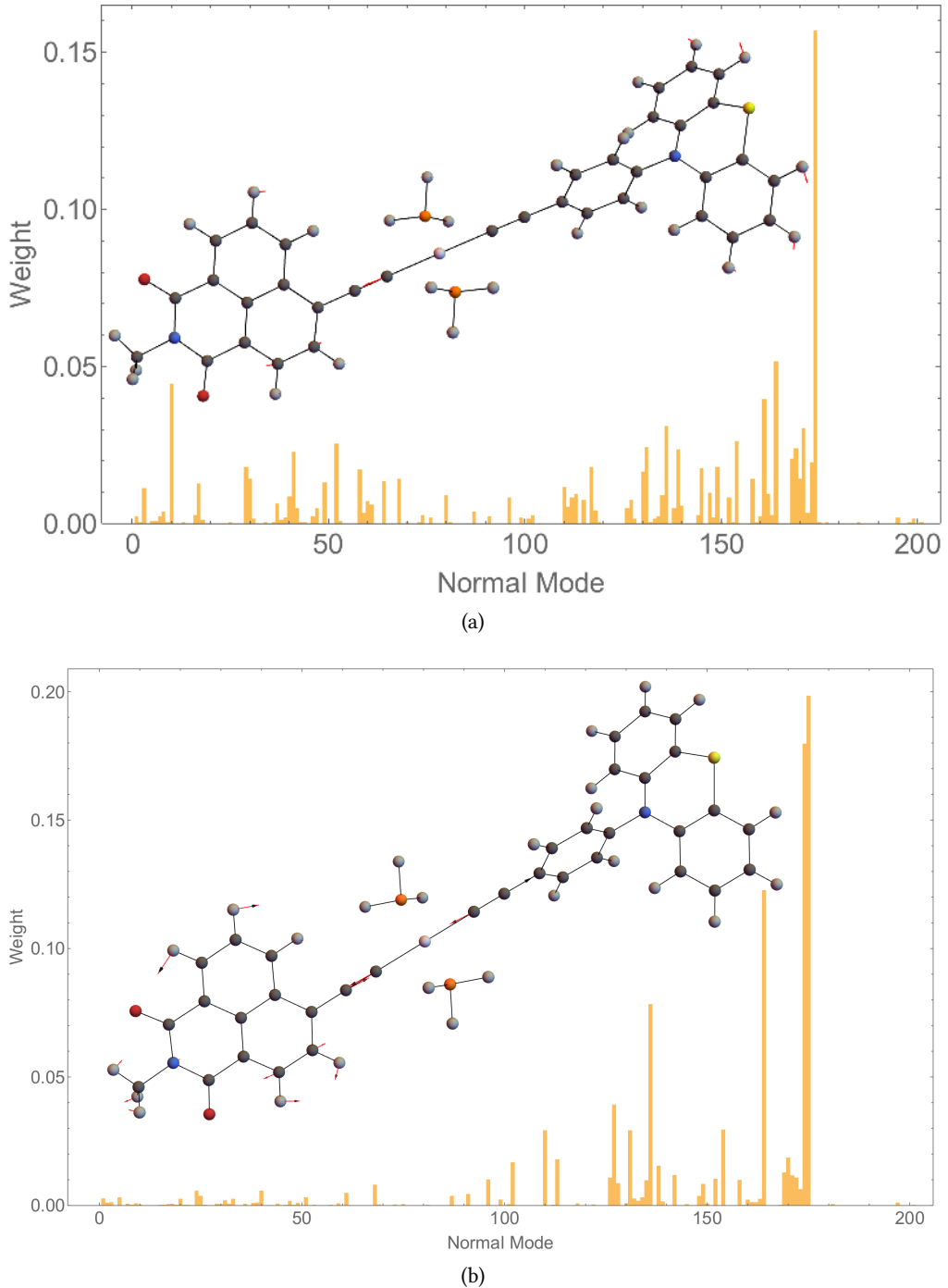


Figure 24.: Projection of primary mode of (a) CSS → ³NAP, (b) CT → ³NAP calculated at ³NAP geometry onto the normal modes of ³NAP. Embedded molecule shows the atomic displacement vectors of primary mode. If we focus on the C≡C bonds, PLMs are like PTZ-Ph-C≡C-Pt-C \rightleftharpoons C-NAP in (a) and PTZ-Ph- $\overset{\leftarrow}{C}\equiv\vec{C}$ -Pt- $\vec{C}\equiv\overset{\leftarrow}{C}$ -NAP in (b).

4.4 RESULTS AND DISCUSSION

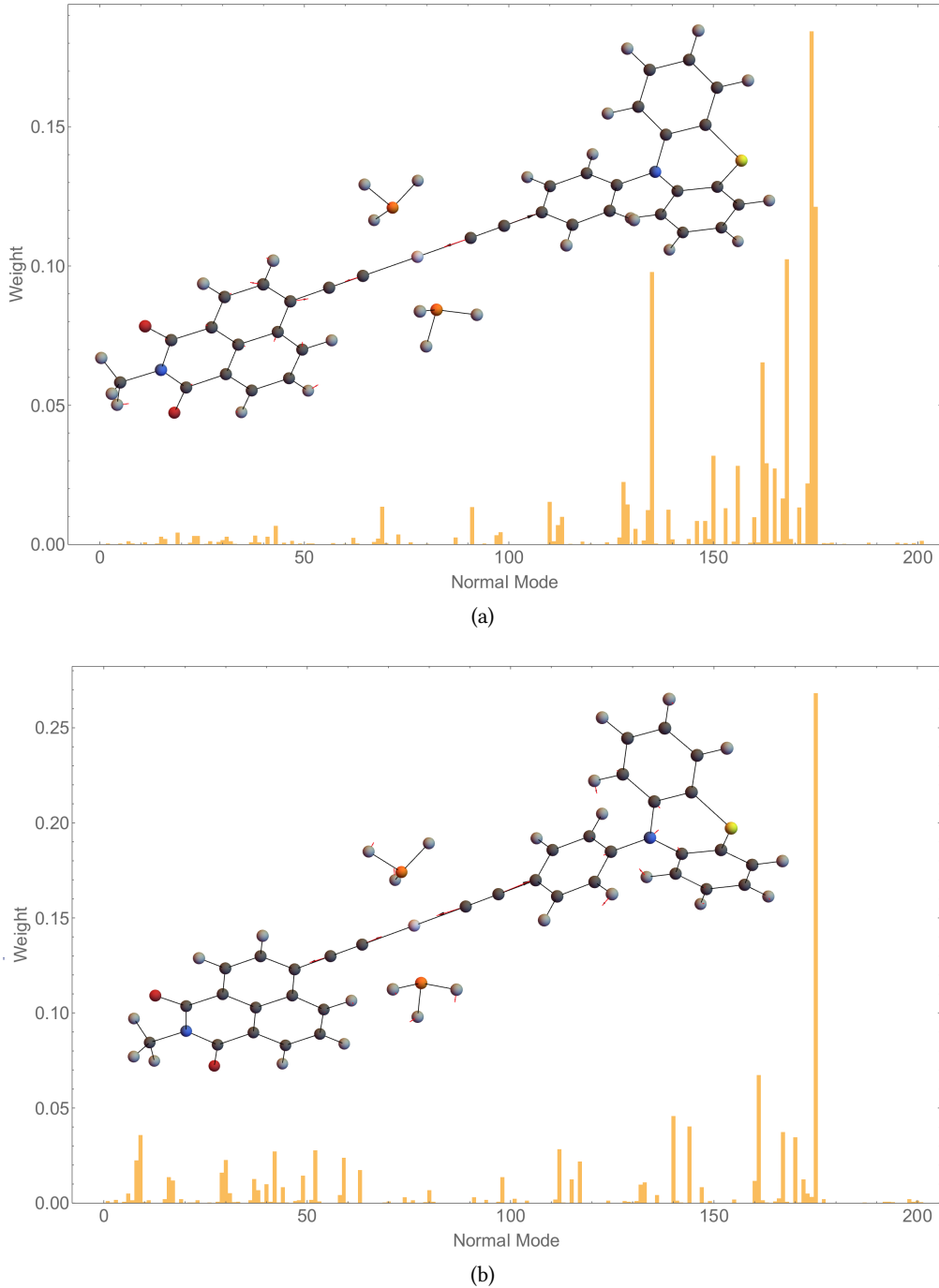


Figure 25.: Projection of primary mode of (a) $\text{CT} \rightarrow {}^3\text{NAP}$, and (b) $\text{CT} \rightarrow \text{CSS}$ calculated at CT geometry onto the normal modes of CT. Embedded molecule shows the atomic displacement vectors of primary mode. If we focus on the $\text{C}\equiv\text{C}$ bonds, PLMs are like $\text{PTZ-Ph}-\overset{\leftarrow}{\text{C}} \equiv \overset{\rightarrow}{\text{C}}-\overset{\leftarrow}{\text{Pt}}-\overset{\rightarrow}{\text{C}} \equiv \overset{\leftarrow}{\text{C}}-\text{NAP}$ in (a) and $\text{PTZ-Ph}-\overset{\leftarrow}{\text{C}} \equiv \overset{\rightarrow}{\text{C}}-\overset{\leftarrow}{\text{Pt}}-\overset{\rightarrow}{\text{C}} \equiv \overset{\leftarrow}{\text{C}}-\text{NAP}$ in (b).

4.4 RESULTS AND DISCUSSION

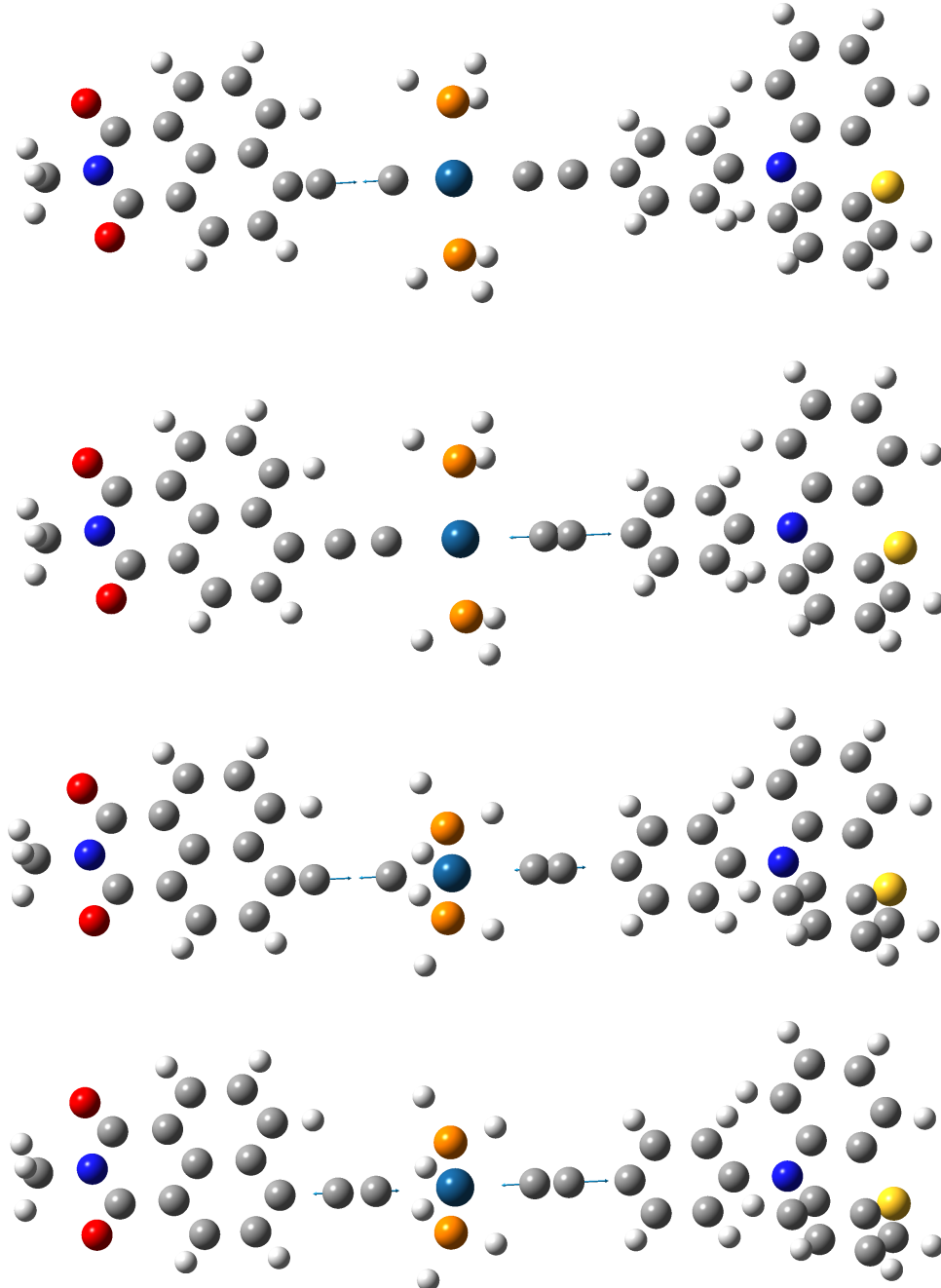


Figure 26.: From top to bottom: the displacement vectors of the 174th, 175th mode of ${}^3\text{NAP}$ state, the 174th, 175th mode of CT state. For clarity, bonds are not shown. They are all the stretching modes of single $\text{C}\equiv\text{C}$ bond, look like PTZ-Ph- $\text{C}\equiv\text{C}$ -Pt- $\overset{\leftrightarrow}{\text{C}}$ -NAP in (a), PTZ-Ph- $\text{C}\equiv\overset{\leftrightarrow}{\text{C}}$ -Pt-C $\equiv\text{C}$ -NAP in (b), PTZ-Ph- $\overset{\leftarrow}{\text{C}}\equiv\overset{\rightarrow}{\text{C}}$ -Pt- $\overset{\leftarrow}{\text{C}}\equiv\overset{\rightarrow}{\text{C}}$ -NAP in (c), and PTZ-Ph- $\overset{\leftarrow}{\text{C}}\equiv\overset{\rightarrow}{\text{C}}$ -Pt- $\overset{\leftarrow}{\text{C}}\equiv\overset{\rightarrow}{\text{C}}$ -NAP in (d).

4.4.3 Condon Approximation

As mentioned above, the results at the CT state, including rate constant and projected modes, are satisfactory, while those at the ${}^3\text{NAP}$ state are poor. The reason is complex. Here we illustrate that the break down of Condon approximation may be one of the causes.

Our model explicitly relies on two assumptions, parabolic assumption and Condon approximation. Parabolic assumption assumes potential energy surface (PES) is parabolic. For this molecule, parabolic assumption is probably true, as the PES has been shown to be parabolic along $\text{C}\equiv\text{C}$ bond in Fig. 20. Condon approximation states that diabatic coupling is independent of nuclear coordinates, i.e., does not change when geometry changes. In Fig. 27 we show the change of diabatic coupling from the ${}^3\text{NAP}$ state to the CT state. It is clear that diabatic couplings do undergo significant changes (note the y axis is logarithmic), especially in the $\text{CSS} \rightarrow {}^3\text{NAP}$ step, where the coupling can differ by two orders of magnitudes. General speaking, Condon approximation fails more near the ${}^3\text{NAP}$ than near the CT state. It may explain why CT geometry gives better results.

To explore the effect of the change of diabatic coupling, we replace the original coupling with the average coupling along interpolation and redo the calculations. The new rate constants are illustrated in Fig. 22, as “with mean V”. The correction brings significant improvements, to both the Marcus and TCLME approaches, at the ${}^3\text{NAP}$ geometry, especially for the most poorly computed $\text{CSS} \rightarrow {}^3\text{NAP}$ transfer.

There is another example to illustrate that the average coupling is a better value to use than the coupling at ${}^3\text{NAP}$ geometry. As we have both ${}^3\text{NAP}$ and CT states optimized, we can compute the energy gap between them. It is 0.81 eV , and is considered to be the best theoretical estimate we can get. We can also use the information at certain geometry to estimate the gap, with parabolic assumption assumed. Certainly how good the estimation is affects the computation of rate constant. Calculating at the CT state gives 0.78 eV , while at the ${}^3\text{NAP}$ geometry gives 0.91 eV . If we still calculate at the ${}^3\text{NAP}$ geometry, but use the average diabatic coupling, the energy gap computed

4.5 CONCLUSION

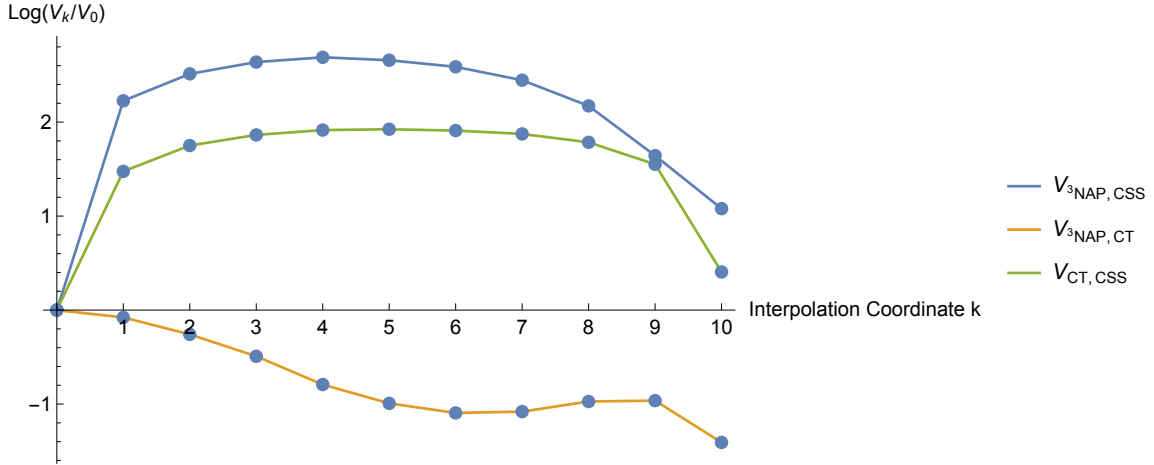


Figure 27.: Diabatic coupling values along the interpolation from the ${}^3\text{NAP} \rightarrow \text{CT}$ geometries. State 0 and 10 stand for the ${}^3\text{NAP}$ and the CT state, respectively.

decreases to 0.85 eV , which is much closer to 0.81 eV . This explains the improvement we get at ${}^3\text{NAP}$ geometry by averaging diabatic coupling.

However, the results at CT geometry get worse, especially for Marcus theory. For the CT \rightarrow CSS reaction, the average diabatic coupling is so unreasonable that Eq. 1.21 does not have any real solution for θ , so it is absent in Fig. 22. Looking at Fig. 27, we suspect that the best choice of diabatic coupling is where Condon approximation holds, i.e., where the change of coupling is slow. The proposition can be tested when the calculations of other two molecules, PTZ-CH₂-Pt-NAP and OMe-PTZ-Pt-NAP are complete.

4.5 CONCLUSION

We present here a modified version of our previous approach [27, 46]. We change the ER diabatization to the GMH approach and apply the model to a much more complex system. Certain success is achieved. Our approach gives reasonable rate constants and always performs better than Marcus theory, which illustrates the robustness of our model.

4.5 CONCLUSION

Weinstein's experiment demonstrates the promising future of IR-controlled electron transfer, which has huge potential in application. The theoretical study is important to understand and predict such property. The results presented here are a blend of success and failure. The calculations based on the CT state give good agreement to experiments, both in rate constant and primary mode. While ³NAP geometry gives much poorer results, but they can be partially corrected by adjusting the diabatic coupling. The cause of failure and success of our method needs more research. The undergoing calculations of other molecules can bring new tests to our method.

Appendices

A

SAMPLE CODES

The codes below are for the computation of rate constants and projected modes, written in Mathematica.

Helper functions

```
ReadRotM[filename_]:= Module[{stream, RotMat},  
  stream = OpenRead[filename];  
  RotMat = Transpose[Partition[ToExpression[Last[Transpose[StringSplit[FindList[filename, "diabatic  
  RotMatrix"]]]]], 2]];  
  Close[stream];  
  Return[RotMat]]  
  
ReadEne[filename_]:= Module[{stream, e1, e2},  
  stream = OpenRead[filename];  
  e1 = ToExpression[Last[StringSplit[Find[stream, "showmatrix adiabatH(0, 0)" ]]]]*27.211396132;  
  e2 = ToExpression[Last[StringSplit[Find[stream, "showmatrix adiabatH(1, 1)" ]]]]*27.211396132 (* in eV*);  
  Close[stream];  
  Return[{e1, e2}] (* in hartree *)]  
  
ReadNormalModes[filename_*]:= Module[{stream, NAtom, NMode, NBlock, Freq, ForceConst,  
  RedMass, IRActive, IRIntens, RamanActive, NormalModeCoord, IAn, AtomicMass, tmp},  
  Freq = {};  
  ForceConst = {};  
  RedMass = {};  
  IRActive = {};  
  IRIntens = {};
```

SAMPLE CODES

```

RamanActive = {};
NormalModeCoord = {};
IAn = {};
AtomicMass = {};

stream = OpenRead[filename];
NMode = ToExpression[Last[Last[StringSplit[FindList[stream, "Mode"]]]]];
NBlock = If[IntegerQ[#, #, Ceiling[#]&[NMode/3];
NAtom = (NMode + 6)/3;
Close[stream];

stream = OpenRead[filename];
Find[stream, "Raman Active"];
Read[stream];
tmp = Table[First[StringSplit[Read[stream, String])), {NAtom}];
AtomicMass = QuantityMagnitude[ElementData[#, "AtomicWeight"] & /@ tmp];
IAn = ElementData[#, "AtomicNumber"] & /@ tmp;
Close[stream];

stream = OpenRead[filename];
Do[
Find[stream, "Mode"];
AppendTo[Freq, ToExpression[Drop[StringSplit[Read[stream, String]], 1]]];
AppendTo[ForceConst, ToExpression[Drop[StringSplit[Read[stream, String]], 2]]];
AppendTo[RedMass, ToExpression[Drop[StringSplit[Read[stream, String]], 2]]];
AppendTo[IRActive, Drop[StringSplit[Read[stream, String]], 2]];
AppendTo[IRIntens, ToExpression[Drop[StringSplit[Read[stream, String]], 2]]];
AppendTo[RamanActive, Drop[StringSplit[Read[stream, String]], 2]];
Read[stream];
NormalModeCoord = Join[NormalModeCoord, ToExpression[Transpose[Table[Partition[Rest[StringSplit[
Read[stream, String]]], 3], {NAtom}]]]];
, {i, 1, NBlock}];
```

SAMPLE CODES

```

Close[stream];

{Freq, ForceConst, RedMass, IRActive, IRIntens, RamanActive} = Flatten /@ {Freq, ForceConst, RedMass,
IRActive, IRIntens, RamanActive};

Return[{NAtom, NMode, AtomicMass, Freq, RedMass, NormalModeCoord}]]

ReadGradient[filename_, NAtom_] := Module[{stream, grad, NMode, NBlock, tmp},
grad = {};
NBlock = If[IntegerQ[#], #, Ceiling[#]]&[NAtom/6];

stream = OpenRead[filename];
Find[stream, "Gradient of the state energy (including CIS Excitation Energy)"];
Do[
Read[stream];
grad = Join[grad, Transpose[Table[ToExpression[Rest[StringSplit[Read[stream, String]]]], {3}]];
, {i, 1, NBlock}];
Return[grad]


---


A_⊗B_:= Outer[Times, A, B]
(* Project1by1 sorts phono modes into a 1 by 1 hierarchical form. Only works for one mode case, for general
3 by 3 case it should be modified. *)
Project1by1[gg_, Hess_]:= Module[
{S, P, Q, PHP, QHQ, L, ωc, ωck, ωb, Mc, Mck, Mb, np, ns, Sinv, G, p, k, g},
(* g should be 1-D, namely, ns = 1 *)
{ns, np} = Dimensions[gg];
g = gg;
ωc = {};
Mc = {};
p = ConstantArray[0, {np, np}];

Do[{
S = Table[g[[i]].g[[j]], {i, ns}, {j, ns}];

```

SAMPLE CODES

```

Sinv = Inverse[S] ;
(* define projection operators *)
P = Sum[Sinv[[i, j]] g[[i]]\[CircleTimes]g[[j]], {i, ns}, {j, ns}] ;
p = p+P; (* $P = P_1 + P_2 + \dots$ *)
Q = IdentityMatrix[np]-p;
PHP = P.Hess.P ;
QHQ = Q.Hess.Q ;
{ωck, Mck} = Chop[Transpose[Take[Sort[Transpose[Eigensystem[PHP]]], -ns]], 10^-8];
{ωb, Mb} = Chop[Transpose[Take[Sort[Transpose[Eigensystem[QHQ]]], ns+k-1-np]], 10^-8];
ωc = Chop[Join[ωc, ωck], 10^-8];
Mc = Chop[Join[Mc, Mck], 10^-8];
ωall= Join[ωc, ωb]//Chop;
M = Join[Mc, Mb]//Chop ;
g = Chop[Join[ConstantArray[0, k], ( M.Hess.Transpose[M])[[k]][[k+1;;np ]]].M], 10^-8]; (* Define nth
mode = (0, 0, 0, ..., γ_{k+1}, γ_{k+2}, ..., γ_{k+N}) *)
Gnew = M.gg[[1]];
}, {k, 1, np-1}];
>(* The kth step gives k*k tridiagonal submatrix on lefttop , diagonal N-k on rightbottom and only the kth
mode is coupled to the N-k bath modes *)

```

```

NMode[n_, hess_, M_, g_]:= Module[{h, gn, Mn, ωprime, Gn},
h = Take[(M.hess.Transpose[M]), {1, n}, {1, n}];
{ωprime, Mn} = Transpose[Sort[Transpose[Eigensystem[h]]]];
gn = Join[Take[g, n], ConstantArray[0, n-Length[Take[g, n]]]];
Gn = Mn.gn;
Return[{Sqrt[ωprime], Gn}]

```

Initialization

- Load Core routines
-

```

SetDirectory[NotebookDirectory[]];
Needs["PhysicalConstants`"]; (* this package is outdated ... but highly useful! *)

```

SAMPLE CODES

- Conversion factors
-

```

hartree = 27.211396132 ElectronVolt (* eV *);
Bohr = 0.5291772108 Angstrom;
hbar = PlanckConstantReduced;

```

- Read in files
-

```

name = {"c13ea", "c13ee", "c14ea", "c14ee", "d26ae", "d26ea", "d26ee", "d27ae", "d27ea", "d27ee", "mmm
"};
path = "qchemout/"<>#.rtf "&/@name;

kkk = 4; (* in this case we are looking at c14ee *)
RotMat = ReadRotM[path[[kkk]]];
Ene = ReadEne[path[[kkk]]];
{NAtom, dof, AtomicMass, AngFreq, RedMass, NormMode} = ReadNormalModes[path[[kkk]]];
Grads = ReadGradient[path[[kkk]], NAtom];
ω = FreqeV = Table[Convert[2Pi SpeedOfLight AngFreq[[i]]Centimeter^-1 PlanckConstantReduced, ElectronVolt
]/ ElectronVolt, {i, 1, dof}];
Freq = Table[Convert[2Pi SpeedOfLight AngFreq[[i]]Centimeter^-1, Second^-1], {i, 1, dof}];
NormModeInMWC = Table[Table[NormMode[[m, i, j]] Sqrt[AtomicMass[[i]]/RedMass[[m]]]//Simplify//Chop, {i,
NAtom}, {j, 3}], {m, 1, dof}];
Force = Table[Sum[NormModeInMWC[[m]][[i, j]]*Grads[[i, j]]/Sqrt[AtomicMass[[i]]//Simplify//Chop, {i, 1,
NAtom}, {j, 1, 3}], {m, 1, dof}];
GGG = CouplingConstant = Table[Convert[Force[[m]]hartree/Bohr PlanckConstantReduced/(2Freq[[m]]AMU),
ElectronVolt/.ElectronVolt->1//Simplify//Chop, {m, 1, dof}];

G = G0 = Table[(
{RotMat[[1, 2]]^2, RotMat[[2, 2]] RotMat[[1, 2]]},
{RotMat[[2, 2]] RotMat[[1, 2]], RotMat[[2, 2]]^2}
)*CouplingConstant[[m]]//Simplify//Chop, {m, 1, dof}];

```

Mode Analysis Routines

- Analyze n projected modes

```
ModeAnalysis[n_]:=Module[{ωprime},
Clear[imax];
imax = n;
{ωprime, g} = NMode[n, hmat, M, Gnew];
Clear[ω, G];
ω = Take[ωprime, imax];
G = Table[(
{RotMat[[1, 2]]^2, RotMat[[2, 2]] RotMat[[1, 2]]},
{RotMat[[2, 2]] RotMat[[1, 2]], RotMat[[2, 2]]^2}
)*g[[m]]//Simplify//Chop, {m, 1, imax}];

v12tab[kkk][imax] = Table[{t, V[1, 2, t]}, {t, 0, nstep*tstep, tstep }];
v21tab[kkk][imax] = Table[{t, V[2, 1, t]}, {t, 0, nstep*tstep, tstep }];
v12[kkk][imax]= Interpolation[v12tab[kkk][imax]];
v21[kkk][imax]= Interpolation[v21tab[kkk][imax]];
b12tab[kkk][imax] = Table[{t, Bd[1, 2, t]}, {t, 0, nstep*tstep, tstep }];
b21tab[kkk][imax] = Table[{t, Bd[2, 1, t]}, {t, 0, nstep*tstep, tstep }];
b12d[kkk][imax]= Interpolation[b12tab[kkk][imax]];
b21d[kkk][imax]= Interpolation[b21tab[kkk][imax]];
```

- Calculation of Correlation Functions

```
nstep = 3000;
tstep = 0.14;
imin = 1;
imax = dof;
Temperature = 298 Kelvin;
```

```
ℏ = ħbar= 6.582122*10^(-4) (* eV/ps^-1 =Convert[PlanckConstantReduced /10^-12 /Second, ElectronVolt]*);
β = Convert[1/(Temperature BoltzmannConstant), ElectronVolt ^-1]/. ElectronVolt ->1;
Clear[ε];
ε[n_]:= Ene[[n]]-Sum[(G[[i, n, n]]^2/ω[[i]]), {i, imin, imax}];
```

SAMPLE CODES

```

nu[i_]:= 1/(\b{Exp}[\beta*\omega[[i]]]-1);

Δ[n_, m_, i_]:= (G[[i, n, n]]-G[[i, m, m]])/\omega[[i]];
Ω[n_, m_, i_]:= (G[[i, n, n]]+G[[i, m, m]])/\omega[[i]];
f[n_, m_, τ_]:= \b{Exp}[-2*\b{Sum}[(nu[i]+0.5)*(Δ[n, m, i])^2*(1-\b{Cos}[\omega[[i]]*τ]), {i, imin, imax}]];
q[n_, m_, τ_]:= \b{Exp}[I*\b{Sum}[(Δ[n, m, i])^2*\b{Sin}[\omega[[i]]*τ], {i, imin, imax}]];
o[n_, m_, τ_]:= (\b{Sum}[G[[i, n, m]]*(Δ[n, m, i]*(nu[i]+1)\b{Exp}[I*\omega[[i]]*τ]-Δ[n, m, i]*nu[i]\b{Exp}[-I*\omega[[i]]*τ]+\Omega[n
, m, i], {i, imin, imax})]^2+\b{Sum}[G[[i, n, m]]*G[[i, m, n]]*((nu[i]+1)\b{Exp}[I*\omega[[i]]*τ]+nu[i]\b{Exp}[-I*\omega[[i
]]*τ]), {i, imin, imax}];

V[m_, n_, τ_]:= 2*f[n, m, τ]*Re[\b{Exp}[-I*(ε[n]-ε[m])*τ]*q[n, m, τ]*o[n, m, τ]];
Bd[m_, n_, τ_]:= f[n, m, τ]*q[n, m, τ]*o[n, m, τ];

```

Get G and [Omega]

```

hess = FreqeV^2;
hmat = \b{DiagonalMatrix}[hess];
Project1by1[{CouplingConstant}, hmat]; (*This gives a fully sorted tridiagonal matrix. You may encounter
singular matrix error for certain molecules, c14ee for example, because some couplings are zero.
Manually abort it and continue.*)

```

```
ModeAnalysis[dof](*Exact calculation *)
```

```

ModeAnalysis[1](*Do however many modes you like.*)
ModeAnalysis[4]
ModeAnalysis[7]
Do[ModeAnalysis[i], {i, 5, 20, 5}]

```

Rate

```

φ12 = \b{Table}[\b{NIntegrate}[v12[kkk][dof][τ], {τ, i*tstep, (i+1)*tstep}], {i, 0, nstep-1}];
φ21 = \b{Table}[\b{NIntegrate}[v21[kkk][dof][τ], {τ, i*tstep, (i+1)*tstep}], {i, 0, nstep-1}];
Ww12 = {{0, 0}};
Ww21 = {{0, 0}};

```

SAMPLE CODES

```

 $\omega\omega_{12} = 0;$ 
 $\omega\omega_{21} = 0;$ 
Do[ $\omega\omega_{12p} = \omega\omega_{12} + \phi_{12}[[i]]$ ];
Ww12 = Append[Ww12, {i*tstep*\hbar,  $\omega\omega_{12p}$ }];
 $\omega\omega_{12} = \omega\omega_{12p}$ , {i, nstep}]];
Do[ $\omega\omega_{21p} = \omega\omega_{21} + \phi_{21}[[i]]$ ];
Ww21 = Append[Ww21, {i*tstep*\hbar,  $\omega\omega_{21p}$ }];
 $\omega\omega_{21} = \omega\omega_{21p}$ , {i, nstep}]];
W12t= Interpolation[Ww12];
W21t= Interpolation[Ww21];
vm12 = Mean@Take[Table[Ww12[[i]][[2]], {i, 1, nstep}], -30];
vm21 = Mean@Take[Table[Ww21[[i]][[2]], {i, 1, nstep}], -100];
W12 = Function[Piecewise[{{W12t#[], 0 <= # <= nstep*tstep}, {vm12, # > nstep*tstep*\hbar}}]];
W21 = Function[Piecewise[{{W21t#[], 0 <= # <= nstep*tstep}, {vm21, # > nstep*tstep*\hbar}}]];
Print["Golden rule rate = ", vm21/ $\hbar$ *10^12, "s-1"];

```

Correlation function

```

Plot[{
  Re[b21d[kkk][dof][.001 t/\hbar]],
  Re[b21d[kkk][1][.001 t/\hbar]], Re[b21d[kkk][4][.001 t/\hbar]],
  Re[b21d[kkk][7][.001 t/\hbar]],
  {t, 0, 10},
  PlotRange -> All,
  AspectRatio -> 1,
  PlotStyle -> {{Black, Thick, Dashing[0.01]}, Blue, Green, Red, Purple},
  LabelStyle -> 16,
  AxesLabel -> {"t/fs", "Re(C12(t))"},
  PlotLegends -> Placed[{"Exact", "1 Mode", "4 Modes", "7 Modes", "7 Modes"}, Right],
  Epilog -> {Style[Text[name[[kkk]], {9, -2.5*10^-7}], 24]}}

```

B

SAMPLE Q-CHEM INPUT FOR OPTIMIZATION

\$comment

The Methyl bridged molecule in Closs' experiments

\$end

\$molecule

o 1

C -3.8538411723 -2.4397929441 -0.2781121557
C -2.6207815714 -1.9037013461 -0.4734139868
C -2.3864306630 -0.5209977640 -0.2477143559
C -3.4546034173 0.2880172639 0.1829603594
C -4.7320392836 -0.2990667773 0.3801193342
C -4.9276493381 -1.6247068524 0.1560653966
H -0.3024509496 -0.5683546523 -0.7751799781
H -4.0217865448 -3.4875821104 -0.4521673982
H -1.8043474981 -2.5222185985 -0.8029584594
C -1.1068985254 0.0645757577 -0.4442755934
C -3.2100290334 1.6685575806 0.4067857365
H -5.5453108592 0.3236698503 0.7099474801
H -5.8980548165 -2.0627615681 0.3066037250
C -1.9754255426 2.1967623486 0.2119973310
C -0.8882067521 1.3902355878 -0.2247876885

SAMPLE Q-CHEM INPUT FOR OPTIMIZATION

H -4.0201227615 2.2943197854 0.7388134855
H -1.8094166773 3.2452457114 0.3900327432
C 0.4648757831 2.0479811399 -0.4686532525
H 0.4950776139 2.4209923288 -1.4889882397
H 0.5324729136 2.9277013644 0.1701035540
C 1.6619530477 1.1704072323 -0.22690000915
C 1.9334725816 0.6753392957 1.1275444642
C 2.5701478753 0.8120644520 -1.2545496283
C 3.0136463511 -0.0943373636 1.3997706949
H 1.2470656779 0.9371021780 1.9125081763
C 3.6649890284 0.0340524470 -1.0138483385
H 2.3858709486 1.16740000686 -2.2534553364
C 3.9284765670 -0.4538015803 0.3499986918
H 3.1989258413 -0.4460423990 2.3990713194
H 4.3521430780 -0.2383340085 -1.7891307794
C 5.0815684544 -1.2743390439 0.6174075172
H 5.2167281378 -1.6003331584 1.6494518435
O 5.8753868349 -1.6014149915 -0.2356539868
\$end

\$rem
MEM_TOTAL 2000
MEM_STATIC 800
JOBTYPE OPT
EXCHANGE HF

SAMPLE Q-CHEM INPUT FOR OPTIMIZATION

CORRELATION	NONE (BUILT-IN)
BASIS	6-31G**
CIS_STATE_DERIV	1
CIS_N_ROOTS	3
CIS_SINGLETS	FALSE
CIS_TRIPLETS	TRUE
SCF_CONVERGENCE	10
CIS_CONVERGENCE	10
THRESH	12
MAX_SCF_CYCLES	100
MAX_CIS_CYCLES	100
GEOM_OPT_TOL_GRADIENT	1
GEOM_OPT_TOL_DISPLACEMENT	1
GEOM_OPT_TOL_ENERGY	1
GEOM_OPT_MAX_CYCLES	100
\$end	

C

SAMPLE Q-CHEM INPUT FOR EDMISTON-RUEDENBERG DIABATIZATION AND FORCE CALCULATIONS

\$comment

The Methyl bridged molecule in Closs' experiments

\$end

\$molecule

O 1

C	-3.8419929279	-2.4456821618	-0.2690422332
C	-2.6081579205	-1.9079004937	-0.4533255368
C	-2.3809108010	-0.5226414883	-0.2376504594
C	-3.4569172426	0.2869401485	0.1713299491
C	-4.7349041861	-0.3020181167	0.3573413828
C	-4.9235046075	-1.6301445619	0.1432844555
H	-0.2894381774	-0.5682376025	-0.7380447964
H	-4.0043196036	-3.4959395508	-0.4355464269
H	-1.7857076241	-2.5274829045	-0.7665197945
C	-1.1004513260	0.0648792976	-0.4231050259
C	-3.2195426616	1.6704088468	0.3852245842
H	-5.5547126469	0.3211860290	0.6707161523
H	-5.8948950387	-2.0696487921	0.2854059362

SAMPLE Q-CHEM INPUT FOR EDMISTON-RUEDENBERG DIABATIZATION AND FORCE CALCULATIONS

C -1.9844594898 2.2003668334 0.2016845644
C -0.8891686620 1.3929537380 -0.2131152300
H -4.0359144267 2.2971163665 0.7007106942
H -1.8239466495 3.2513547824 0.3720935397
C 0.4638869377 2.0544918303 -0.4445577994
H 0.4951028424 2.4426504343 -1.4594919837
H 0.5294088124 2.9245121242 0.2080254041
C 1.6613532731 1.1754453019 -0.2133060963
C 1.9372633777 0.6714255815 1.1365768977
C 2.5643452548 0.8222956387 -1.2473216246
C 3.0170728042 -0.1015358081 1.3994301576
H 1.2542282181 0.9292951682 1.9263988906
C 3.6587904111 0.0412588689 -1.0162575132
H 2.3761552339 1.1841586041 -2.2435733502
C 3.9268051190 -0.4552844945 0.3432280438
H 3.2059507180 -0.4599134371 2.3959689767
H 4.3429306322 -0.2278976092 -1.7957176595
C 5.0798545363 -1.2789904248 0.6003230883
H 5.2187252084 -1.6118267753 1.6308432733
O 5.8687826459 -1.6008672566 -0.2594648103

\$end

\$rem

SCF_CONVERGENCE 10
CIS_CONVERGENCE 10

SAMPLE Q-CHEM INPUT FOR EDMISTON-RUEDENBERG DIABATIZATION AND FORCE CALCULATIONS

```
THRESH           12
MAX_SCF_CYCLES 100
MAX_CIS_CYCLES 100
MEM_TOTAL       20000
MEM_STATIC      5000
JOBTYPE         FORCE
SYMMETRY        FALSE
EXCHANGE        HF
CORRELATION     NONE (BUILT-IN)
BASIS           6-31G**
CIS_STATE_DERIV 2
CIS_N_ROOTS    3
CIS_SINGLETS   FALSE
CIS_TRIPLETS   TRUE
SCF_GUESS      READ
$end
```

@@@

\$molecule

read

\$end

\$rem

```
SCF_CONVERGENCE 10
CIS_CONVERGENCE 10
```

SAMPLE Q-CHEM INPUT FOR EDMISTON-RUEDENBERG DIABATIZATION AND FORCE CALCULATIONS

```
THRESH           12
JOBTYPE          SP
EXCHANGE          HF
CIS_N_ROOTS      2
CIS_SINGLETS     FALSE
CIS_TRIPLETS     TRUE
BASIS            6-31G**
SCF_GUESS        READ
SYMMETRY          FALSE
RPA               FALSE
MEM_STATIC        5000
MEM_TOTAL         20000
SYM_IGNORE        TRUE
ER_CIS_NUMSTATE   2
LOC_CIS_OV_SEPARATE TRUE
MAX_SCF_CYCLES    300
MAX_CIS_CYCLES    100
$end
```

```
$localized_diabatization
```

```
comment
```

```
1 2
```

```
$end
```

D

GAUSSIAN INPUT FOR THE CSS STATE OF PTZ-PT-NAP

```
# td=(triplets,nstates=10) b3lyp/genecp scrf=(solvent=dichloromethane) geom=connectivity
int=ultrafine scf=tight
```

CSS state

o 3

Pt	-1.24471	-0.26354	0.20032
C	-3.23857	-0.33229	0.26656
C	0.77522	-0.20111	0.13446
P	-1.08794	-2.34278	1.23001
P	-1.27148	1.8192	-0.83379
C	-4.48372	-0.39764	0.30924
C	2.00323	-0.15792	0.09985
C	3.4297	-0.10502	0.0638
C	4.20623	-0.87193	0.95838
C	4.10009	0.71856	-0.86652
C	5.59665	-0.81322	0.92523
H	3.70791	-1.5109	1.68074
C	5.49051	0.77122	-0.89936
H	3.51902	1.31453	-1.56333

GAUSSIAN INPUT FOR THE CSS STATE OF PTZ-PT-NAP

C	6.24862	0.00699	-0.00158
H	6.18899	-1.40332	1.61786
H	5.99429	1.40729	-1.62131
C	-6.26305	1.49542	-1.11445
C	-5.86305	-0.49231	0.37134
C	-6.73967	0.44456	-0.32737
C	-7.14824	2.37548	-1.77229
C	-6.4677	-1.55842	1.1576
C	-8.15894	0.27683	-0.20365
C	-8.51666	2.21932	-1.65507
H	-6.74267	3.18203	-2.37638
C	-7.81683	-1.69972	1.26333
H	-5.7999	-2.24617	1.66714
C	-9.03225	1.165	-0.8672
C	-8.69345	-0.78471	0.58577
H	-9.21223	2.8847	-2.15286
H	-8.26228	-2.4932	1.85144
C	-10.49207	1.01206	-0.75424
C	-10.13332	-0.9578	0.71408
C	-12.40027	-0.2414	0.17939
H	-12.68501	-1.22301	-0.20805
H	-12.89858	0.54515	-0.38182
N	-10.9546	-0.04646	0.03562
O	-10.64432	-1.86417	1.38855
O	-11.28016	1.77378	-1.32362

GAUSSIAN INPUT FOR THE CSS STATE OF PTZ-PT-NAP

C	8.34212	1.11679	0.65108
C	8.37799	-0.77205	-0.94552
C	9.71301	1.02984	0.9681
C	7.65564	2.28643	1.01794
C	9.75164	-1.04223	-0.78095
C	7.72385	-1.34025	-2.05146
C	10.37411	2.09314	1.58644
C	8.31358	3.32925	1.67243
H	6.5991	2.38035	0.79972
C	10.44605	-1.81588	-1.71328
C	8.41521	-2.14602	-2.95776
H	6.6665	-1.15987	-2.20107
C	9.67676	3.24552	1.95269
H	11.43543	2.00176	1.80017
H	7.74981	4.21502	1.95123
H	11.50844	-1.99037	-1.56734
C	9.78036	-2.3825	-2.8015
H	7.87614	-2.57862	-3.79586
N	7.68802	0.04108	-0.00703
S	10.59122	-0.49601	0.69269
H	-5.19124	1.63036	-1.2193
H	10.19361	4.05988	2.45119
H	10.32309	-2.99973	-3.51093
H	-0.33303	-2.39422	2.41525
H	-2.27623	-2.98011	1.62655

GAUSSIAN INPUT FOR THE CSS STATE OF PTZ-PT-NAP

H	-0.46756	-3.35507	0.47631
H	-0.59951	1.90902	-2.06568
H	-2.51348	2.39523	-1.15208
H	-0.65825	2.86433	-0.12023
H	-12.67851	-0.19213	1.23483

H C N O P S o

6-31G(d)

Pt o

SDD

Pt

SDD

BIBLIOGRAPHY

- [1] Rudolph A Marcus. On the theory of oxidation-reduction reactions involving electron transfer. I. *The Journal of Chemical Physics*, 24(5):966–978, 1956.
- [2] Rudolph A Marcus. On the theory of electron-transfer reactions. VI. unified treatment for homogeneous and electrode reactions. *The Journal of Chemical Physics*, 43(2):679–701, 1965.
- [3] Rudolph A Marcus. Electron transfer reactions in chemistry. Theory and experiment. *Reviews of Modern Physics*, 65(3):599, 1993.
- [4] Andrey Pereverzev and Eric R Bittner. Time-convolutionless master equation for mesoscopic electron-phonon systems. *The Journal of Chemical Physics*, 125(10):104906, 2006.
- [5] Hiroyuki Tamura, John GS Ramon, Eric R Bittner, and Irene Burghardt. Phonon-driven ultrafast exciton dissociation at donor-acceptor polymer heterojunctions. *Physical Review Letters*, 100(10):107402, 2008.
- [6] Hiroyuki Tamura, Eric R Bittner, and Irene Burghardt. Exciton dissociation at donor-acceptor polymer heterojunctions: Quantum nonadiabatic dynamics and effective-mode analysis. *The Journal of Chemical Physics*, 126(2):021103, 2007.
- [7] Eric R Bittner and Carlos Silva. Noise-induced quantum coherence drives photo-carrier generation dynamics at polymeric semiconductor heterojunctions. *Nature Communications*, 5, 2014.

BIBLIOGRAPHY

- [8] Jaykrishna Singh, Eric R Bittner, David Beljonne, and Gregory D Scholes. Fluorescence depolarization in poly[2-methoxy-5-((2-ethylhexyl)oxy)-1, 4-phenylenevinylene]: Sites versus eigenstates hopping. *The Journal of Chemical Physics*, 131(19):194905, 2009.
- [9] Morgan Kennedy Grover and R Silbey. Exciton–phonon interactions in molecular crystals. *The Journal of Chemical Physics*, 52(4):2099–2108, 1970.
- [10] MJ Rice and Yu N Gartstein. Excitons and interband excitations in conducting polymers based on phenylene. *Physical Review Letters*, 73(18):2504, 1994.
- [11] Clyde Edmiston and Klaus Ruedenberg. Localized atomic and molecular orbitals. *Reviews of Modern Physics*, 35(3):457, 1963.
- [12] Wolfgang Domcke, David R Yarkony, KÅ Horst, et al. *Conical intersections: electronic structure, dynamics and spectroscopy*, volume 15. World Scientific, 2004.
- [13] C Alden Mead and Donald G Truhlar. Conditions for the definition of a strictly diabatic electronic basis for molecular systems. *The Journal of Chemical Physics*, 77(12):6090–6098, 1982.
- [14] Andrey Pereverzev, Eric R Bittner, and Irene Burghardt. Energy and charge-transfer dynamics using projected modes. *The Journal of Chemical Physics*, 131(3):034104, 2009.
- [15] Etienne Gindensperger, Irene Burghardt, and Lorenz S Cederbaum. Short-time dynamics through conical intersections in macrosystems. I. Theory: Effective-mode formulation. *The Journal of Chemical Physics*, 124(14):144103, 2006.
- [16] Etienne Gindensperger, Irene Burghardt, and Lorenz S Cederbaum. Short-time dynamics through conical intersections in macrosystems. II. Applications. *The Journal of Chemical Physics*, 124(14):144104, 2006.

BIBLIOGRAPHY

- [17] Lorenz S Cederbaum, Etienne Gindensperger, and Irene Burghardt. Short-time dynamics through conical intersections in macrosystems. *Physical Review Letters*, 94(11):113003, 2005.
- [18] JR Miller, LT Calcaterra, and GL Closs. Intramolecular long-distance electron transfer in radical anions. The effects of free energy and solvent on the reaction rates. *Journal of the American Chemical Society*, 106(10):3047–3049, 1984.
- [19] Joseph E Subotnik, Sina Yeganeh, Robert J Cave, and Mark A Ratner. Constructing diabatic states from adiabatic states: Extending generalized Mulliken–Hush to multiple charge centers with boys localization. *The Journal of Chemical Physics*, 129(24):244101, 2008.
- [20] Joseph E Subotnik, Robert J Cave, Ryan P Steele, and Neil Shenvi. The initial and final states of electron and energy transfer processes: Diabatization as motivated by system-solvent interactions. *The Journal of Chemical Physics*, 130(23):234102, 2009.
- [21] Joseph E Subotnik, Josh Vura-Weis, Alex J Sodt, and Mark A Ratner. Predicting accurate electronic excitation transfer rates via Marcus theory with Boys or Edmiston-Ruedenberg localized diabatization†. *The Journal of Physical Chemistry A*, 114(33):8665–8675, 2010.
- [22] David L Dexter. A theory of sensitized luminescence in solids. *The Journal of Chemical Physics*, 21(5):836–850, 1953.
- [23] Y. Shao, Z. Gan, E. Epifanovsky, A. T. B. Gilbert, M. Wormit, J. Kussmann, A. W. Lange, A. Behn, J. Deng, X. Feng, D. Ghosh, M. Goldey, P. R. Horn, L. D. Jacobson, I. Kaliman, R. Z. Khaliullin, T. Kús, A. Landau, J. Liu, E. I. Proynov, Y. M. Rhee, R. M. Richard, M. A. Rohrdanz, R. P. Steele, E. J. Sundstrom, H. L. Woodcock III, P. M. Zimmerman, D. Zuev, B. Albrecht, E. Alguire, B. Austin, G. J. O. Beran, Y. A. Bernard, E. Berquist, K. Brandhorst, K. B. Bravaya, S. T. Brown, D. Casanova, C.-M. Chang, Y. Chen, S. H. Chien, K. D. Closser, D. L. Crittenden, M. Diedenhofen, R. A. DiStasio Jr., H. Dop, A. D. Dutoi, R. G. Edgar, S. Fatehi, L. Fusti-Molnar, A. Ghysels, A. Golubeva-Zadorozhnaya, J. Gomes, M. W. D. Hanson-Heine, P. H. P. Harbach,

BIBLIOGRAPHY

- A. W. Hauser, E. G. Hohenstein, Z. C. Holden, T.-C. Jagau, H. Ji, B. Kaduk, K. Khistyayev, J. Kim, J. Kim, R. A. King, P. Klunzinger, D. Kosenkov, T. Kowalczyk, C. M. Krauter, K. U. Lao, A. Laurent, K. V. Lawler, S. V. Levchenko, C. Y. Lin, F. Liu, E. Livshits, R. C. Lochan, A. Luenser, P. Manohar, S. F. Manzer, S.-P. Mao, N. Mardirossian, A. V. Marenich, S. A. Maurer, N. J. Mayhall, C. M. Oana, R. Olivares-Amaya, D. P. O'Neill, J. A. Parkhill, T. M. Perrine, R. Peverati, P. A. Pieniazek, A. Prociuk, D. R. Rehn, E. Rosta, N. J. Russ, N. Sergueev, S. M. Sharada, S. Sharmaa, D. W. Small, A. Sodt, T. Stein, D. Stück, Y.-C. Su, A. J. W. Thom, T. Tsuchimochi, L. Vogt, O. Vydrov, T. Wang, M. A. Watson, J. Wenzel, A. White, C. F. Williams, V. Vanovschi, S. Yeganeh, S. R. Yost, Z.-Q. You, I. Y. Zhang, X. Zhang, Y. Zhou, B. R. Brooks, G. K. L. Chan, D. M. Chipman, C. J. Cramer, W. A. Goddard III, M. S. Gordon, W. J. Hehre, A. Klamt, H. F. Schaefer III, M. W. Schmidt, C. D. Sherrill, D. G. Truhlar, A. Warshel, X. Xua, A. Aspuru-Guzik, R. Baer, A. T. Bell, N. A. Besley, J.-D. Chai, A. Dreuw, B. D. Dunietz, T. R. Furlani, S. R. Gwaltney, C.-P. Hsu, Y. Jung, J. Kong, D. S. Lambrecht, W. Liang, C. Ochsenfeld, V. A. Rassolov, L. V. Slipchenko, J. E. Subotnik, T. Van Voorhis, J. M. Herbert, A. I. Krylov, P. M. W. Gill, and M. Head-Gordon. Advances in molecular quantum chemistry contained in the Q-Chem 4 program package. *Molecular Physics*, 113:184–215, 2015.
- [24] Gerhard L Closs, Piotr Piotrowiak, Jean M MacInnis, and Graham R Fleming. Determination of long-distance intramolecular triplet energy-transfer rates. Quantitative comparison with electron transfer. *Journal of the American Chemical Society*, 110(8):2652–2653, 1988.
- [25] Gerhard L Closs and John R Miller. Intramolecular long-distance electron transfer in organic molecules. *energy*, 3:3, 1988.
- [26] Gerhard L Closs, Mark D Johnson, John R Miller, and Piotr Piotrowiak. A connection between intramolecular long-range electron, hole, and triplet energy transfers. *Journal of the American Chemical Society*, 111(10):3751–3753, 1989.

BIBLIOGRAPHY

- [27] Xunmo Yang and Eric R Bittner. Intramolecular charge- and energy-transfer rates with reduced modes: Comparison to Marcus theory for donor–bridge–acceptor systems. *The Journal of Physical Chemistry A*, 118(28):5196–5203, 2014.
- [28] Jens Ulstrup and Joshua Jortner. The effect of intramolecular quantum modes on free energy relationships for electron transfer reactions. *The Journal of Chemical Physics*, 63(10):4358–4368, 1975.
- [29] Joel N Schrauben, Kevin L Dillman, Warren F Beck, and James K McCusker. Vibrational coherence in the excited state dynamics of cr (acac)₃: probing the reaction coordinate for ultrafast intersystem crossing. *Chemical Science*, 1(3):405–410, 2010.
- [30] Daly Davis, Maytal Caspary Toroker, Shammai Speiser, and Uri Peskin. On the effect of nuclear bridge modes on donor–acceptor electronic coupling in donor–bridge–acceptor molecules. *Chemical Physics*, 358(1):45–51, 2009.
- [31] Don Devault. Quantum mechanical tunnelling in biological systems. *Quarterly Reviews of Biophysics*, 13(04):387–564, 1980.
- [32] Harry B Gray and Jay R Winkler. Electron transfer in proteins. *Annual Review of Biochemistry*, 65:537–561, 1996.
- [33] Frederick D Lewis, Jianqin Liu, Wilfried Weigel, Wolfgang Rettig, Igor V Kurnikov, and David N Beratan. Donor-bridge-acceptor energetics determine the distance dependence of electron tunneling in dna. *Proceedings of the National Academy of Sciences*, 99(20):12536–12541, 2002.
- [34] Ch Bressler, C Milne, V-T Pham, A ElNahhas, RM Van der Veen, W Gawelda, S Johnson, P Beaud, D Grolimund, M Kaiser, et al. Femtosecond xanes study of the light-induced spin crossover dynamics in an iron (ii) complex. *Science*, 323(5913):489–492, 2009.

BIBLIOGRAPHY

- [35] Crystal Shih, Anna Katrine Museth, Malin Abrahamsson, Ana Maria Blanco-Rodriguez, Angel J Di Bilio, Jawahar Sudhamsu, Brian R Crane, Kate L Ronayne, Mike Towrie, Antonín Vlček, et al. Tryptophan-accelerated electron flow through proteins. *Science*, 320(5884):1760–1762, 2008.
- [36] Jascha Repp, Peter Liljeroth, and Gerhard Meyer. Coherent electron-nuclear coupling in oligothiophene molecular wires. *Nature Physics*, 6(12):975–979, 2010.
- [37] Alexei Halpin, Philip JM Johnson, Roel Tempelaar, R Scott Murphy, Jasper Knoester, Thomas LC Jansen, and RJ Dwayne Miller. Two-dimensional spectroscopy of a molecular dimer unveils the effects of vibronic coupling on exciton coherences. *Nature Chemistry*, 6(3):196–201, 2014.
- [38] Miguel A Soler, Tammie Nelson, Adrian E Roitberg, Sergei Tretiak, and Sebastian Fernandez-Alberti. Signature of nonadiabatic coupling in excited-state vibrational modes. *The Journal of Physical Chemistry A*, 118(45):10372–10379, 2014.
- [39] Spiros S Skourtis, David H Waldeck, and David N Beratan. Inelastic electron tunneling erases coupling-pathway interferences. *The Journal of Physical Chemistry B*, 108(40):15511–15518, 2004.
- [40] Dequan Xiao, Spiros S Skourtis, Igor V Rubtsov, and David N Beratan. Turning charge transfer on and off in a molecular interferometer with vibronic pathways. *Nano Letters*, 9(5):1818–1823, 2009.
- [41] David N Beratan, Spiros S Skourtis, Ilya A Balabin, Alexander Balaeff, Shahar Keinan, Ravindra Venkatramani, and Dequan Xiao. Steering electrons on moving pathways. *Accounts of Chemical Research*, 42(10):1669–1678, 2009.

BIBLIOGRAPHY

- [42] P Antoniou, Z Ma, P Zhang, David N Beratan, and SS Skourtis. Vibrational control of electron-transfer reactions: a feasibility study for the fast coherent transfer regime. *Physical Chemistry Chemical Physics*, 17(46):30854–30866, 2015.
- [43] Milan Delor, Paul A Scattergood, Igor V Sazanovich, Anthony W Parker, Gregory M Greetham, Anthony JHM Meijer, Michael Towrie, and Julia A Weinstein. Toward control of electron transfer in donor-acceptor molecules by bond-specific infrared excitation. *Science*, 346(6216):1492–1495, 2014.
- [44] Milan Delor, Theo Keane, Paul A Scattergood, Igor V Sazanovich, Gregory M Greetham, Michael Towrie, Anthony JHM Meijer, and Julia A Weinstein. On the mechanism of vibrational control of light-induced charge transfer in donor–bridge–acceptor assemblies. *Nature Chemistry*, 2015.
- [45] Paul A Scattergood, Milan Delor, Igor V Sazanovich, Oleg V Bouganov, Sergei A Tikhomirov, Alexander S Stasheuski, Anthony W Parker, Gregory M Greetham, Michael Towrie, E Stephen Davies, et al. Electron transfer dynamics and excited state branching in a charge-transfer platinum (ii) donor–bridge–acceptor assembly. *Dalton Transactions*, 43(47):17677–17693, 2014.
- [46] Xunmo Yang and Eric R Bittner. Computing intramolecular charge and energy transfer rates using optimal modes. *The Journal of Chemical Physics*, 142(24):244114, 2015.
- [47] Robert J Cave and Marshall D Newton. Generalization of the mulliken-hush treatment for the calculation of electron transfer matrix elements. *Chemical Physics Letters*, 249(1):15–19, 1996.
- [48] Robert J Cave and Marshall D Newton. Calculation of electronic coupling matrix elements for ground and excited state electron transfer reactions: comparison of the generalized mulliken–hush and block diagonalization methods. *The Journal of Chemical Physics*, 106(22):9213–9226, 1997.

BIBLIOGRAPHY

- [49] M. J. Frisch, G. W. Trucks, H. B. Schlegel, G. E. Scuseria, M. A. Robb, J. R. Cheeseman, G. Scalmani, V. Barone, B. Mennucci, G. A. Petersson, H. Nakatsuji, M. Caricato, X. Li, H. P. Hratchian, A. F. Izmaylov, J. Bloino, G. Zheng, J. L. Sonnenberg, M. Hada, M. Ehara, K. Toyota, R. Fukuda, J. Hasegawa, M. Ishida, T. Nakajima, Y. Honda, O. Kitao, H. Nakai, T. Vreven, J. A. Montgomery, Jr., J. E. Peralta, F. Ogliaro, M. Bearpark, J. J. Heyd, E. Brothers, K. N. Kudin, V. N. Staroverov, R. Kobayashi, J. Normand, K. Raghavachari, A. Rendell, J. C. Burant, S. S. Iyengar, J. Tomasi, M. Cossi, N. Rega, J. M. Millam, M. Klene, J. E. Knox, J. B. Cross, V. Bakken, C. Adamo, J. Jaramillo, R. Gomperts, R. E. Stratmann, O. Yazyev, A. J. Austin, R. Cammi, C. Pomelli, J. W. Ochterski, R. L. Martin, K. Morokuma, V. G. Zakrzewski, G. A. Voth, P. Salvador, J. J. Dannenberg, S. Dapprich, A. D. Daniels, Ö. Farkas, J. B. Foresman, J. V. Ortiz, J. Cioslowski, and D. J. Fox. Gaussian 09 Revision E.01. Gaussian Inc. Wallingford CT 2009.
- [50] Tian Lu and Feiwu Chen. Multiwfn: a multifunctional wavefunction analyzer. *Journal of Computational Chemistry*, 33(5):580–592, 2012.